TAD boundary architecture and gene activity are uncoupled

Faisal Almansour[1], Nadezda A. Fursova[2], Adib Keikhosravi[3], Kathleen S. Metz Reed[1], Daniel R. Larson[2], Gianluca Pegoraro[3] and Tom Misteli[1]

[1]Cell Biology of Genomes Group, National Cancer Institute, NIH, Bethesda MD 20892, USA
[2]Systems Biology of Gene Expression, National Cancer Institute, NIH, Bethesda MD 20892, USA
[3]High-throughput Imaging Facility, National Cancer Institute, NIH, Bethesda MD 20892, USA

Correspondence: mistelit@mail.nih.gov

Keywords: Genome organization, topologically associating domains, transcription, high-throughput imaging

ABSTRACT

Topologically associating domains (TADs) are prominent features of genome organization. A proposed function of TADs is to contribute to gene regulation by promoting chromatin interactions within a TAD and by suppressing interactions between TADs. Here, we directly probe the structure-function relationship of TADs by simultaneously assessing TAD boundary architecture and gene activity at the single-cell and -allele level using high-throughput imaging. We find that while TAD boundaries pair more frequently than non-boundary regions, these interactions are infrequent and are uncorrelated with transcriptional activity of genes within the TAD. Similarly, acute global transcriptional inhibition or gene-specific activation does not alter TAD boundary proximity. Furthermore, disruption of TAD boundaries by depletion of the architectural chromatin protein CTCF is insufficient to alter expression of genes within the TAD. These results suggest that TAD boundary architecture and gene activity are largely uncoupled.

INTRODUCTION

Beyond the linear DNA sequence, genomes are folded into higher-order structures[1]. Some of the most prominent genome features are chromatin loops and domains. Chromatin conformation mapping techniques — most notably Hi-C and Micro-C — have particularly highlighted topologically associating domains (TADs) as ubiquitous architectural features of higher eukaryotic genomes[2-5].

TADs are self-assembling, contiguous genomic regions which preferentially interact with each other rather than with neighboring regions, creating distinct chromatin domains[3]. In human cells, TADs are typically 0.2-1 Mb in size and are defined by flanking boundary regions, which are marked by binding sites for the CTCF (CCCTC-binding factor) protein[3, 6, 7]. TADs form via a process referred to as loop extrusion, which is driven by the cohesin complex association with DNA, and by its ATP-driven motor activity, which reels in DNA until it encounters bound CTCF molecules at the TAD boundaries, thus forming a domain[6-8].

TADs are thought to have a gene regulatory function by bringing control elements, such as enhancers, over large genomic distances into physical proximity to their target genes within the same TAD, while at the same time limiting their interactions with genes in other TADs[2, 4]. This model is in line with the known role of CTCF as an insulation factor (9, 10). A regulatory role for TADs is also supported by the observation that targeted deletions or inversions of boundary elements alter enhancer-promoter communication and, in some cases, gene expression[11-13]. Furthermore, comparative mapping of the *Ubx* and *AbdA* TADs in Drosophila embryos showed that a ~2-fold change in enhancer-gene contact frequency leads to a ~7-fold difference in gene expression[14]. Disruption of TAD boundaries has also been linked to human disease, as structural variations that alter domain architecture can cause pathogenic rewiring of enhancer-gene contacts, for example, in cancers, and in neurological and congenital disorders[15]. Moreover, mutations in components of the cohesin complex cause developmental disorders, known as cohesinopathies, such as Cornelia de Lange syndrome, in which impaired chromatin architecture and altered transcriptional regulation are thought to drive the phenotype[16].

On the other hand, several lines of evidence suggest TADs are not strictly required for

transcription regulation. Global removal of cohesin or CTCF produces surprisingly modest effects on genome-wide transcription, suggesting that most genes can be expressed relatively accurately without intact TAD structures[17, 18]. Although many CTCF and cohesin binding sites overlap with enhancers and promoters, a substantial fraction does not, indicating that domain boundaries are not universally tied to regulatory elements[19-21]. Furthermore, in *Drosophila*, large-scale rearrangements of TADs often lead to only modest transcriptional changes, and enhancer hijacking events appear relatively rare[22]. In addition, cis-regulatory transcription hubs form before TAD establishment and prior to transcriptional activation, indicating that gene regulatory contacts may emerge independently of domain architecture[23]. Similarly, during dorsoventral patterning in *Drosophila*, tissue-specific gene expression patterns emerge despite largely invariant TADs across tissues[24]. Finally, in mammals, enhancer–promoter contacts persist even after the global loss of CTCF or cohesin, underscoring that regulatory interactions can be maintained without stable TAD anchoring[25-28]. These observations point to a limited functional role of TAD architecture in gene regulation.

A confounding factor in assessing the functional role of TADs on gene regulation is the recent realization that TAD structure is highly dynamic, resulting in variable TAD conformations in individual cells and alleles[29-32]. High-throughput DNA FISH studies indicate that TAD boundary pairing only occurs in typically 5-20% of alleles at any given time in a population[31]. In agreement, live cell imaging demonstrates that TAD boundaries undergo continuous motion, and that the persistence time of pairing is on the order of ~10–30 minutes before they separate again, consistent with polymer simulations of cohesin-mediated loops[32, 33]. In addition to the variable nature of TAD architecture, gene expression itself is similarly dynamic, with most genes undergoing rapid cycles of activity and inactivity, referred to as gene bursting[34, 35]. Furthermore, recent observations point to a bidirectional relationship in which transcriptional activity itself also affects chromatin structure[27, 36-38]. Neither the variability in TAD organization nor the dynamics of gene activity is captured by commonly used population-based profiling methods, confounding the assessment of the effect of TAD structure on gene expression at the level of individual alleles.

Here, we directly probe the structure-function relationship of TADs at the single-cell and single-allele level by use of high-throughput imaging to simultaneously visualize TAD boundary architecture by DNA-FISH and nascent RNA production by RNA-FISH. Using the TADs containing the *EGFR* and *MYC* genes, respectively, as model systems, we quantitatively compare boundary distances at individual active and inactive alleles or upon transcriptional perturbation or stimulation. Conversely, we probe the effect of loss of the architectural TAD protein CTCF on gene expression. In all comparisons, we find that TAD boundary architecture is unrelated to gene activity.

RESULTS

Simultaneous assessment of TAD boundary structure and gene activity by high-throughput imaging

To quantitatively analyze the relationship between TAD boundary structure and gene activity at the single-cell and single-allele level, we developed a high-throughput FISH imaging (HiFISH) and image analysis pipeline[39, 40] comprised of three components: 1) detection of TAD boundaries and nascent RNA using combined DNA- and RNA-FISH in a 384-well high-throughput format[39] (DNA/RNA HiFISH), 2) measurement of center-to-center TAD boundary distances using HiTIPS, a customized image analysis software to probe features of nuclear architecture[40], and 3) quantitative comparison of boundary distances and gene expression status at each visualized allele (**Figure 1A;** see Materials and Methods). DNA/RNA HiFISH was either performed simultaneously in a single hybridization step or in two sequential steps, yielding comparable results as previously described[39]. Similar results were obtained using 2D maximum-intensity projections or 3D imaging[41] (see below).

The combined DNA/RNA HiFISH imaging approach resulted in robust simultaneous detection of TAD boundaries and nascent RNA in multiple cell types[39] (**Figure 1B** and see below). The correct number of DNA FISH signals was routinely detected in >95% of cells in non-transformed hTERT-HFFc6 fibroblasts (HFF) or in human bronchial epithelial cells (HBEC) as previously reported[39]. Similarly, the detected RNA-FISH signals accurately reflected the number of active alleles as demonstrated by comparison with the number of active *MYC* alleles visualized by live-cell imaging using an MS2-tagged *MYC* reporter system in HBECs (**Figure 1C**). The high detection efficiency underscores the sensitivity and specificity of our approach for probing TAD boundary architecture and nascent transcription at the single-cell and single-allele level[39]. The high-throughput nature of this approach enabled routine probing of thousands of individual alleles per experimental condition, providing high statistical power in comparative analyses.

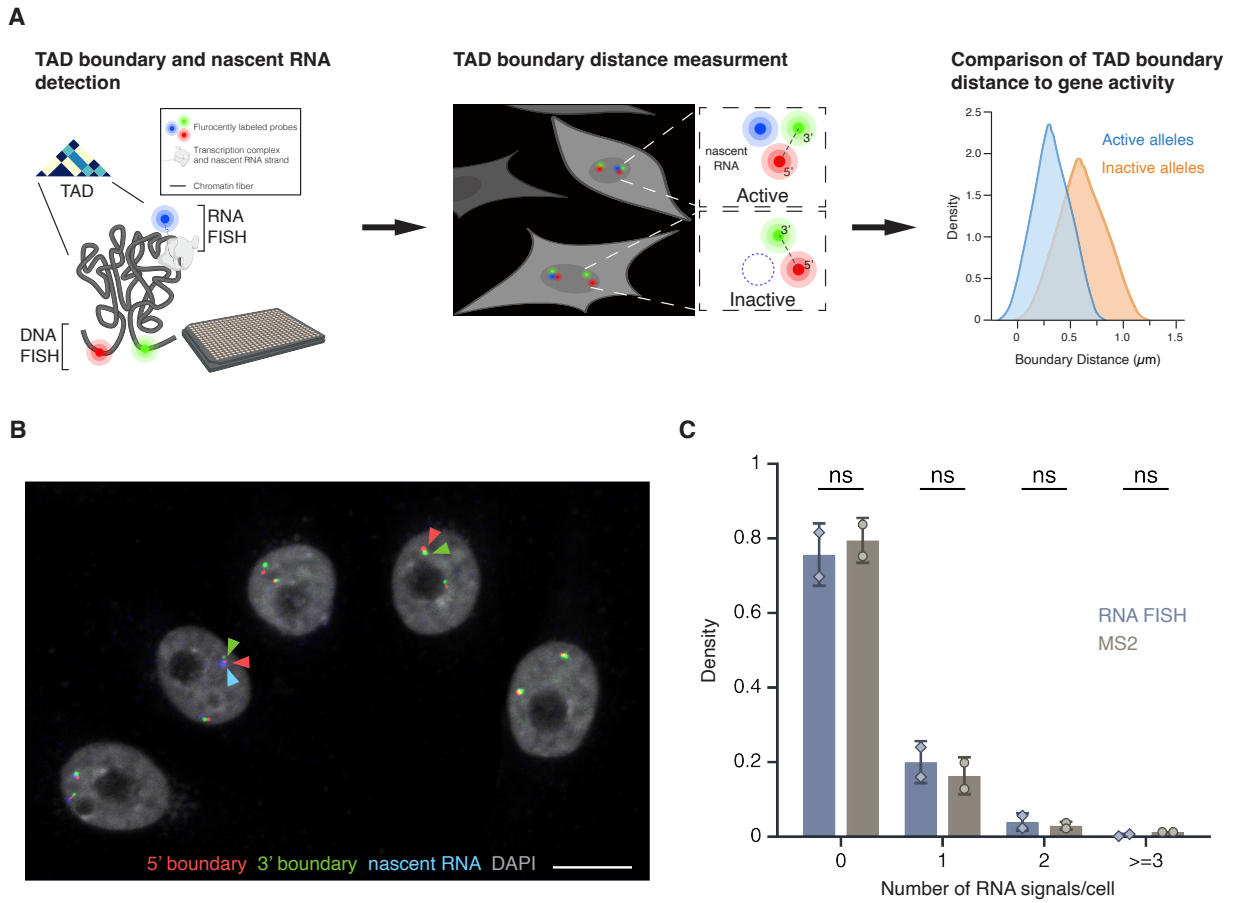

Figure 1. High-throughput DNA/RNA FISH

(A) *Schematic overview of the HiFISH pipeline used to simultaneously measure TAD boundary distance and gene activity at the single-cell and single-allele levels. Step 1: Design of DNA FISH probes based on Micro-C profiling and detection of DNA and nascent RNA by HiFISH. Step 2: Measurement of center-to-center TAD boundary distances and RNA signal at individual alleles by image analysis using HiTIPS[40]. Step 3: Quantitative comparison of TAD boundary distances with gene activity at each allele.*

(B) *DNA/RNA HiFISH detection of 5' (green) and 3' (red) MYC TAD boundaries and nascent RNA (blue) in HBEC cells. Scale bar: 10 μm.*

(C) *Quantification of MYC nascent RNA signals using DNA/RNA HiFISH in fixed HBEC cells or a MS2-tagged MYC reporter in living HBEC cells. Bars represent means +/- SEM from two experiments. Dots indicate means from individual experiments. 166,953 cells were analyzed for MS2, and 30,137 cells for DNA/RNA HiFISH. Statistical significance was calculated using two-way ANOVA with Bonferroni correction: ns, not significant ($p \geq 0.05$).*

Selection and validation of TAD models

Two TADs containing the *EGFR* and *MYC* genes, respectively, were selected as models for our analysis based on the high biological relevance in signaling and transcription, respectively, of the two genes and their presence in structurally well-defined TADs, as mapped by high-resolution (1 kb) publicly available Micro-C datasets of HFF cells[42] and human embryonic stem cells (ESCs)[43]. Both TADs are conserved in both cell types and display well-defined corner peaks and side streaks, both hallmarks of stable and structurally distinct TADs[42, 43].

The *EGFR* TAD spans ~500 kb and has two sub-TADs of ~250 kb each, while the *MYC* TAD extends over ~3 Mb and comprises two large sub-TADs (~1 Mb and ~2 Mb, respectively) (**Figure 2A**). The *MYC* TAD is more insulated from flanking chromatin than the *EGFR* TAD, which itself may reside in a sub-TAD within a broader domain not visible at lower Hi-C resolution[42, 43]. The two TADs also differ in their gene content and chromatin landscape based on ChromHMM analysis[44] (**Supplementary Figure 1**), with the *EGFR* TAD enriched in transcriptionally active regions, while the *MYC* TAD is predominantly quiescent, with isolated active chromatin features clustered near the long noncoding RNAs *PVT1* and *PCAT1.* The *MYC* TAD contains only two protein-coding genes, *MYC* and *POU5F1B,* and multiple noncoding elements (**Supplementary Figure 1**). The *MYC* gene lies close to the 5′ boundary, while *POU5F1B* is within the upstream sub-TAD. The *EGFR* TAD harbors three protein-coding genes—*EGFR*, *LANCL2*, and *VOPP1*—with the *EGFR* gene positioned relatively distally upstream (**Supplementary Figure 1**). The fraction of the TAD covered by each gene also varies: *EGFR* occupies ~40% of its TAD, whereas *LANCL2* and *VOPP1* cover ~17% and ~20%, respectively. In contrast, *MYC* and *POU5F1B* together span less than 1% of the *MYC* TAD (**Supplementary Figure 1**). The *MYC* and *EGFR* TAD boundaries lie in largely quiescent chromatin, with the exception of the 3′ *EGFR* TAD boundary, which contains some active marks due to the proximity to the *EGFR gene* (**Supplementary Figure 1**). The differences in size and variation in structural and functional features between the two TADs make them attractive and robust models for investigating the relationship between TAD boundary structure and gene activity at single-allele resolution.

To detect the *EGFR* and *MYC* TAD boundaries, we selected specific BAC DNA FISH probes that directly target the 5' and 3' boundaries, respectively (**Figure 2A, Supplementary Figures 1–2**). To control for regional variability and to distinguish boundary-specific behavior from broader chromatin effects, control DNA FISH probes targeting non-TAD control regions were also used. These probes were positioned on the same chromosome arm, equidistant upstream of the respective 5′ TAD boundaries and located within the same or adjacent cytogenetic bands (**Figure 2A**, **Supplementary Figures 1–2**). The *EGFR*-associated non-TAD control region contains one protein-coding gene and fewer noncoding elements relative to its corresponding TAD boundary (**Supplementary Figure 1**). In contrast, the *MYC* non-TAD control region contains more genes and exhibits a more complex local topology, bordering multiple looped domains and small TADs (**Supplementary Figure 1**). Both non-TAD regions share a relatively quiescent chromatin state, with sparse transcriptional and regulatory element enrichment. Consistent with their function as boundaries, Micro-C contact frequencies were at least 10-fold higher for the *MYC* and *EGFR* TAD boundary regions compared to the corresponding control regions (**Figure 2A**).

TAD boundaries pair at low frequency

We first used DNA/RNA HiFISH to determine the distance distribution profiles and interaction frequencies of TAD boundaries at the single-allele level[39] (**Figure 2B–E**) (see Materials and Methods). As expected, the median distance for *MYC* TAD boundaries was smaller compared to non-TAD regions in both HFF (0.41 ± 0.30 μm vs 0.81 ± 0.63 μm; median ± Inter Quartile Range) and HBEC (0.46 ± 0.33 μm vs 0.71 ± 0.50 μm; Mann-Whitney U test, $p < 1\times10^{-10}$ for both) (**Figure 2D–E**). Similarly, in HFF, *EGFR* TAD boundaries were in closer proximity than non-TAD regions (0.41 ± 0.30 μm vs. 0.56 ± 0.48 μm; U test, $p < 1\times10^{-20}$) (**Figure 2D**). Interestingly, the *EGFR* TAD boundaries showed a more uniform distribution in HBEC, with TAD boundaries showing a similar distribution to non-TAD regions (0.39 ± 0.28 μm vs 0.42 ± 0.29 μm; U test, $p < 0.01$) (**Figure 2C**). The lack of a strong difference in proximity for *EGFR* boundaries in HBECs likely reflects the smaller size of the *EGFR* TAD (~0.5 Mb) (**Figure 2A**; **Supplementary Figure 1)** and the smaller nuclear size in HBECs (**Figure 2C**).

To quantify the pairing frequency of *MYC* and *EGFR* TAD boundaries, we calculated the percentage of alleles with TAD boundary distances below a 250 nm threshold, a value previously used to define chromatin interactions[31, 32]. *EGFR* TAD boundaries were within 250 nm in 31 ± 14% (Mean ± SD) of alleles in HBECs and 33 ± 17% in HFF, and *MYC* TAD boundaries were within this range in 23 ± 9% of HBEC and 27 ± 9% of HFF alleles (**Figure 2B–C**). Non-TAD control regions showed lower interaction frequencies with 27 ± 13% and 20 ± 8% for *EGFR* in HBEC and HFF, respectively, and 8 ± 1% and 6 ± 0.3% for *MYC* in HBEC and HFF (**Figure 2B–C;** $p < 0.05$ for all comparisons). As previously noted, while adjusting the distance threshold changes the absolute percentage of close contacts, it does not affect the relative differences between TAD boundaries and non-TAD regions[31]. These results are consistent with single-cell FISH and Hi-C studies showing that TAD boundaries pair two- to threefold more frequently than non-TAD regions, and with live-cell imaging studies showing transient boundary pairing [30-32, 45-50]. Our findings confirm that TAD boundaries exhibit higher interaction frequencies and shorter distances than non-TAD regions, but that boundary pairing is a relatively infrequent and transient event.

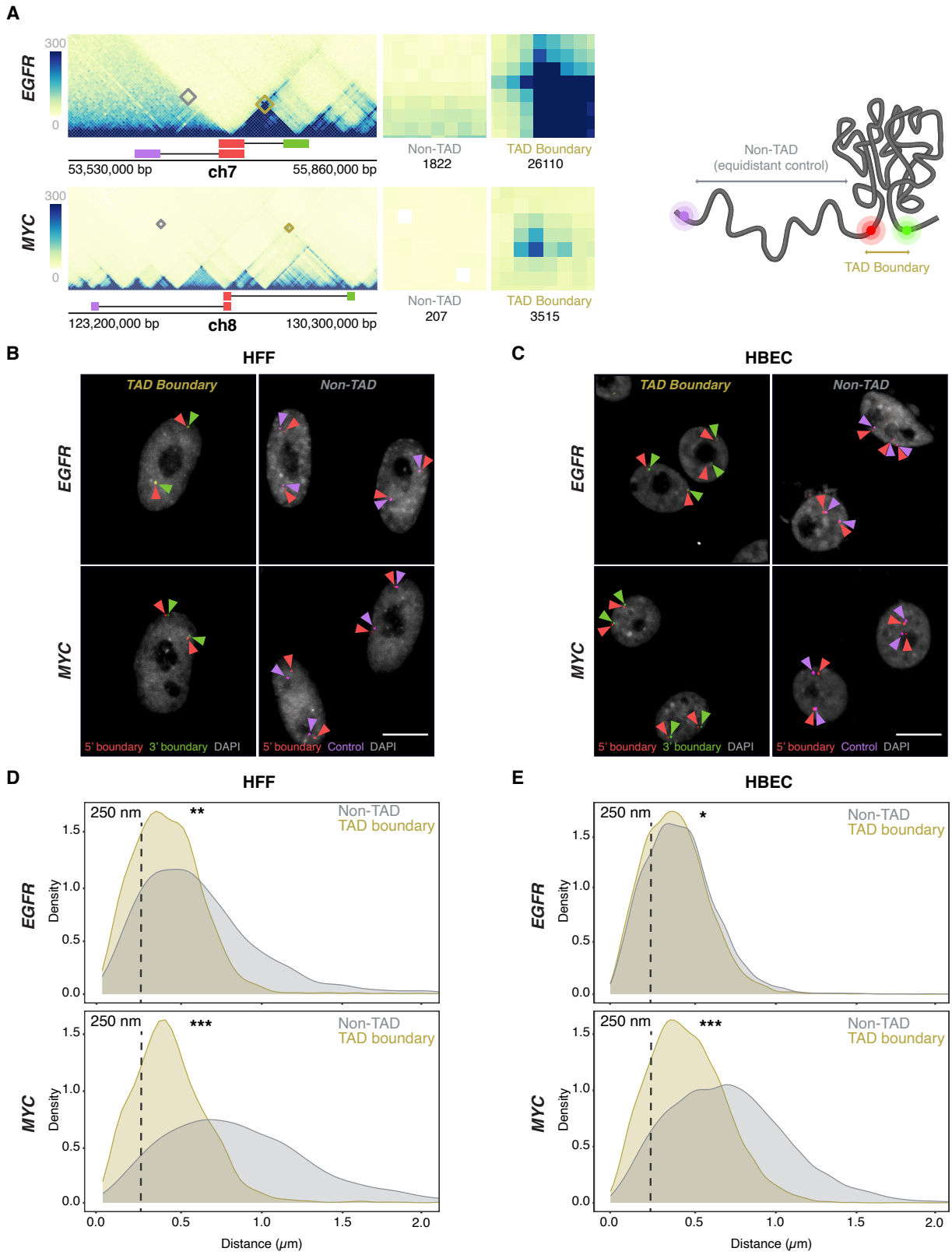

Figure 2. TAD boundaries interact more frequently than non-TAD regions

(A) *Micro-C contact maps for* EGFR *and* MYC *TADs and adjacent regions in HFF cells, highlighting TAD boundaries and genomically equidistant non-TAD regions. Squares denote the probe positions used for 3' (green), 5' boundary (red), and equidistant non-TAD controls (purple). Interactions between the 5' TAD boundaries and the 3' TAD (yellow) or non-TAD boundaries (grey) are highlighted and total Micro-C contacts between regions are quantified, emphasizing high TAD boundary contact frequency in both* EGFR *and* MYC *TADs, as well as weaker signals in the non-TAD regions.*
(B-C) *Representative DNA HiFISH images of* EGFR *and* MYC *TAD boundary and non-TAD regions in HFF (B) and HBEC (C). Scale bar: 10 µm.*
(D-E) *Measurement of boundary distances. Distance distributions of* EGFR *and* MYC *TAD boundaries versus matched non-TAD regions in HFF (D) and HBEC (E) cells. Dashed line indicates 250nm threshold used to define physical interaction. Between 2,000 and 18,000 alleles were analyzed per sample. Values represent an individual dataset from a single experiment of multiple experiments. Mann-Whitney U test p-values are: *** $p < 1\times10^{-100}$; ** $1\times10^{-100} \leq p < 1\times10^{-20}$; * $1\times10^{-20} \leq p < 0.01$.*

TAD boundary distance is not related to gene activity status

To assess whether TAD boundary architecture correlates with gene activity at the single-allele level, boundary distances were compared between transcriptionally active and inactive alleles using high-throughput DNA/RNA HiFISH (**Figure 3A**). Active alleles were identified by the presence of nascent RNA FISH signals in the proximity (< 1 µm) of a TAD boundary signal (see Materials and Methods), while inactive alleles lacked detectable RNA signals near TAD boundary signals (**Figure 1A, 3A**). RNA detection was efficient, as indicated by the comparable number of active transcription sites detected by RNA-FISH as in living cells using the MS2-RNA detection system (**Figure 1C**).

Comparative analyses of multiple independent DNA/RNA HiFISH experiments - each comprising up to 20,000 alleles - revealed no consistent difference in TAD boundary distances between active and inactive alleles of *EGFR* and *MYC* loci in HBEC, HFF, and HCT116 cells (**Figure 3B–E**; **Supplementary Figure 3A**). In HBECs, *EGFR* boundary distances were identical between active (0.29 ± 0.07 µm, mean of medians ± SD) and inactive (0.29 ± 0.07 µm) alleles (Mann-Whitney U test, p = 0.57) (**Figure 3B**). Similarly,

in HFF, both active and inactive *EGFR* alleles exhibited identical boundary distances (0.32 ± 0.08 μm; p = 0.75) (**Figure 3C**). A similar pattern was observed for *MYC*. In HBECs, median boundary distances were 0.39 ± 0.05 μm for active *MYC* alleles and 0.37 ± 0.06 μm for inactive alleles (p = 0.31) (**Figure 3D**). In HFFs, active and inactive *MYC* alleles also had similar distances (0.39 ± 0.04 μm vs. 0.41 ± 0.04 μm; p = 0.46) (**Figure 3E**). A similar pattern was observed for both genes in HCT116 (**Supplementary Figure 3C**). Furthermore, the TAD boundary distances of the two alleles in the same nucleus were uncorrelated (**Supplementary Figure 3B)** and not significantly different between active or inactive alleles, either as measured by 2D or 3D imaging (**Supplementary Figure 3B-C**). Taken together, these results indicate that the proximity of *MYC* and *EGFR* TAD boundaries is not related to gene activity at individual alleles.

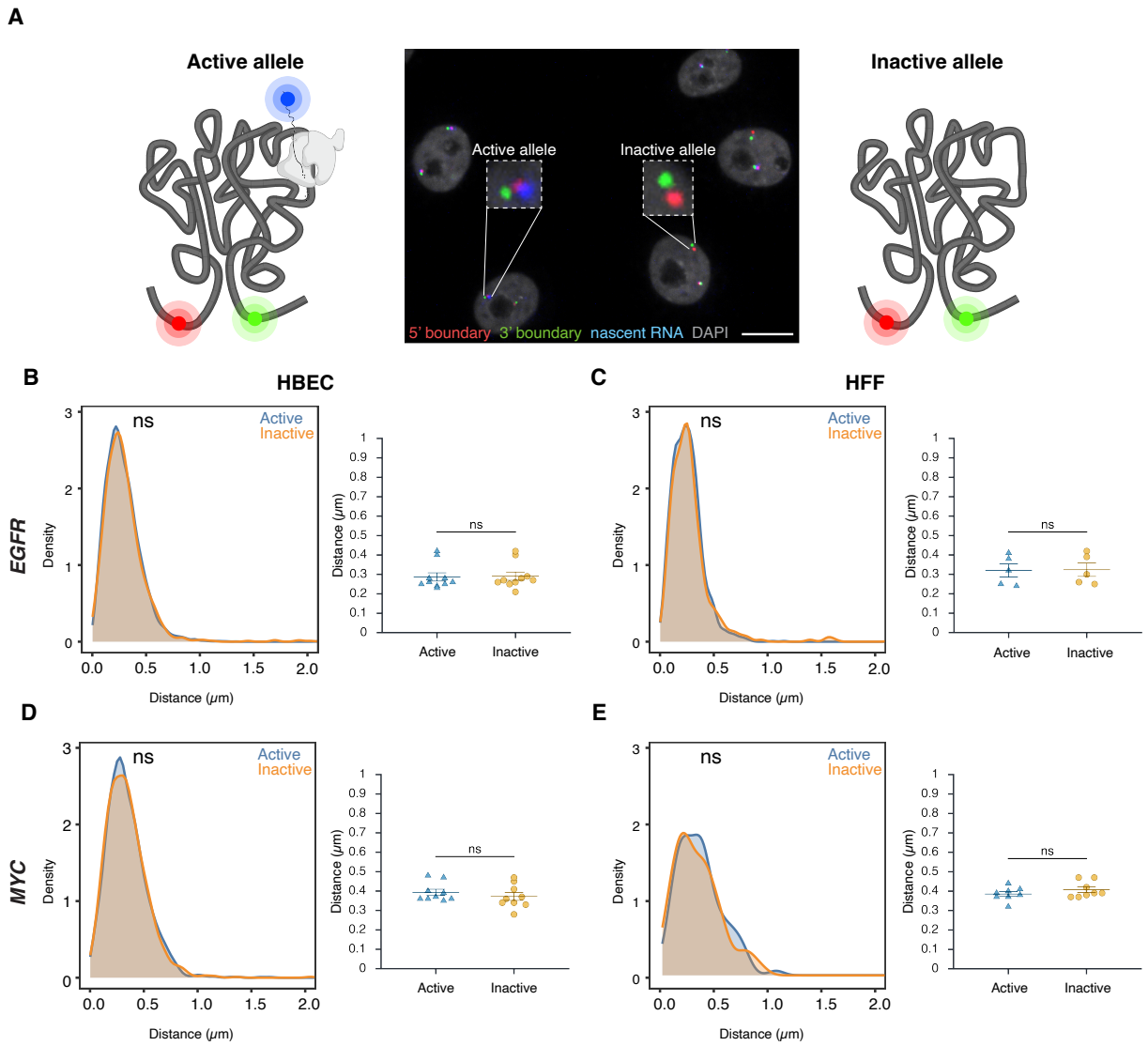

Figure 3. TAD boundary proximity is not related to gene activity status

(A) *Representative DNA/RNA HiFISH image of* EGFR *nascent RNA (blue) and its associated 5' (red) and 3' (green) TAD boundaries in HBECs, illustrating detection of active (RNA-positive) and inactive (RNA-negative) alleles. Scale bar: 10 μm.*

(B–E) *Comparison of TAD boundary distances for EGFR and MYC alleles based on transcriptional activity status. Histograms of allele-specific distance distributions from a representative dataset from a single experiment; Mann–Whitney U test p-values are indicated as follows: ns, not significant (p ≥ 0.05). Dot plots of the mean of median distances from multiple experiments (500–20,000 alleles per condition); Error bars represent SEM and statistical significance was calculated using two-way ANOVA with Bonferroni correction: ns, not significant (p ≥ 0.05).*

Inhibition of gene activity does not alter TAD boundary pairing

To further test the relationship of TAD boundary architecture with gene activity, we assessed whether acute global transcriptional inhibition affects TAD boundary structure. We treated HBEC or HFF cells with 5,6-dichlorobenzimidazole 1-β-D-ribofuranoside (DRB), an inhibitor of CDK9 and CDK7 that acutely blocks RNA polymerase II (RNAPII) transcription elongation and initiation[51, 52]. As expected, after 2 hours of DRB treatment, nascent RNA signals for *EGFR* and *MYC* decreased by over 90%, confirming effective transcriptional inhibition (**Figure 4A**).

TAD boundary distances remained unchanged for both *EGFR* and *MYC* upon transcriptional inhibition (**Figure 4B**). In HBEC and HFF cells, *EGFR* TAD boundary median distances were similar in untreated controls (0.31 ± 0.10 μm and 0.31 ± 0.10 μm; mean of medians ± SD) and DRB-treated cells (0.30 ± 0.11 μm and 0.31 ± 0.11 μm; U-test p-values = 0.51 and 1.00, respectively). Likewise, *MYC* TAD boundary distances showed minimal changes in HBEC (0.38 ± 0.07 μm control vs. 0.37 ± 0.08 μm treated; p = 0.83) nor in HFF (0.37 ± 0.07 μm control vs. 0.35 ± 0.08 μm treated; p = 0.83) (**Figure 4B**). Transcriptional inhibition also did not affect the distance distribution of non-TAD control regions (**Supplementary Figure 4**). These results indicate that acute inhibition of global RNAPII-dependent transcription does not significantly impact the structural organization of TAD boundaries, suggesting that the architecture of TAD boundaries is uncoupled from short-term gene expression dynamics.

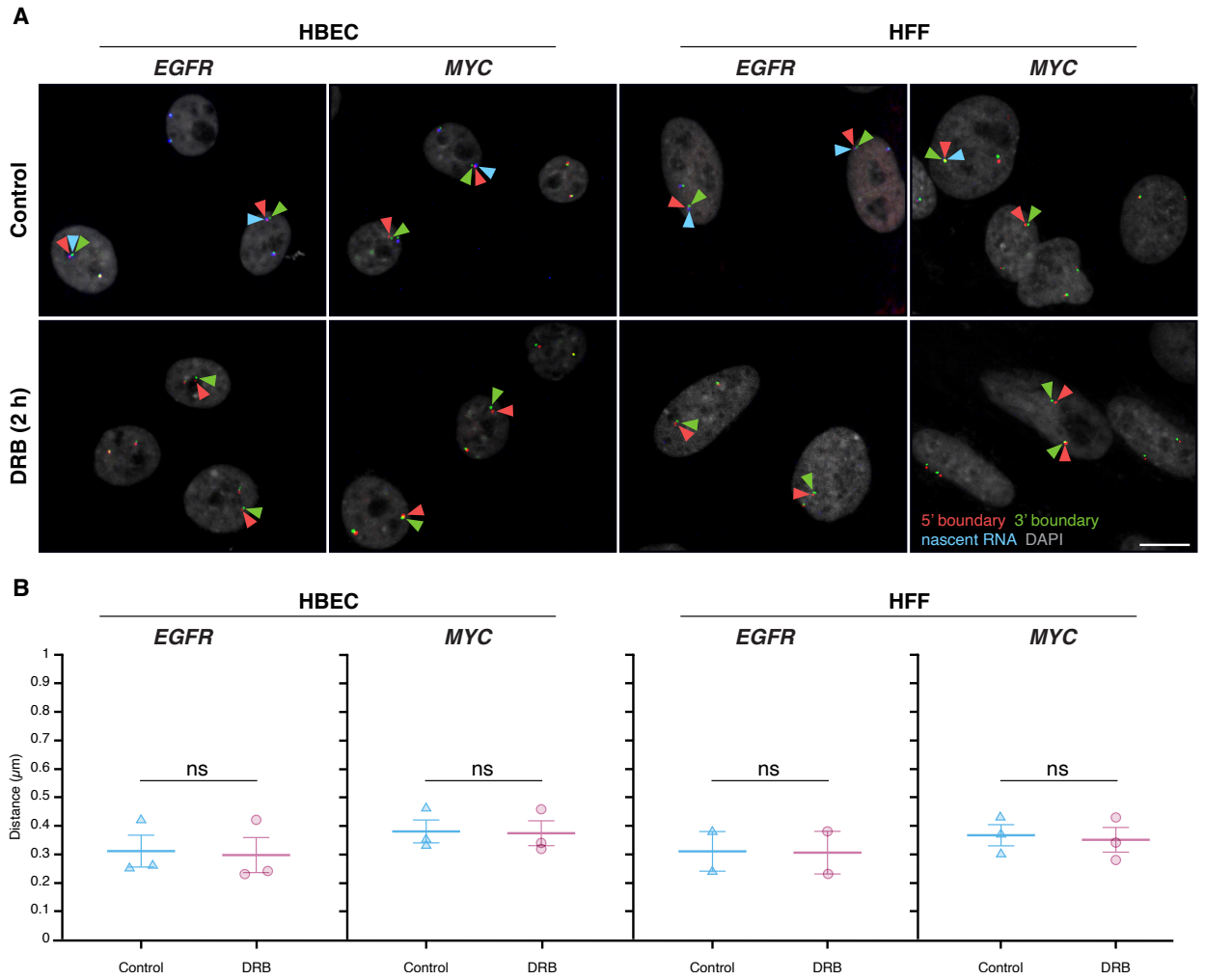

Figure 4. Global transcription inhibition does not alter TAD boundary pairing

(A) *Representative RNA HiFISH images of* MYC *nascent RNA in HBECs with and without 2-hour DRB treatment. Scale bars: 10 μm.*

(B) *Quantification of TAD boundary distances for* EGFR *and* MYC *in the presence or absence of DRB. Dot plots of the mean of median distances from multiple experiments (500–20,000 alleles per condition). Error bars represent SEM. Statistical significance was calculated using two-way ANOVA with Bonferroni correction: ns, not significant (p ≥ 0.05).*

boundaries and non-TAD regions for the *ERRFI1*, *FKBP5, and VARS2 TADs* revealed more similar interaction frequencies between TAD boundaries compared to equidistant non-TAD control regions (**Figure 5A**). Accordingly, DNA FISH showed a more uniform distribution of TAD boundary distances for the Dex-inducible *ERRFI1*, *FKBP5*, and *VARS2* TADs in HBEC compared to the Dex non/mildly inducible *MYC* and *EGFR* TADs

Stimulating gene activity does not change TAD boundary distances

To conversely assess whether transcriptional activation influences TAD boundary structure, HBEC cells were treated for two hours with dexamethasone (Dex), a glucocorticoid receptor (GR) agonist known to selectively induce GR-target genes (53). We selected for this analysis *ERRFI1*, *FKBP5, and VARS2*, which are all robustly induced (2- to 7-fold) as measured by RNA-seq (**Supplementary Figure 5A**) and reside in relatively large TADs of 400, 1000, and 700 kb, respectively (**Figure 5A**). Interestingly, unlike the TADs for the Dex-insensitive *MYC* and *EGFR* genes, Micro-C maps of the TAD (**Figure 5B**). Distances for TAD boundaries were 0.31 ± 0.01 μm, (mean of medians ± SD) 0.40 ± 0.02 μm, and 0.35 ± 0.01 μm for *ERRFI1*, *FKBP5*, and *VARS2*, respectively, and were comparable to those for non-TAD regions (0.28 ± 0.00 μm, 0.40 ± 0.01 μm, and 0.39 ± 0.00 μm). Statistical comparison by Bonferroni's multiple-comparison test of TAD vs non-TAD distances showed no significant difference for *ERRFI1* ($p = 0.1572$, ns) or *FKBP5* ($p = 1.0000$, ns), but a modest yet significant difference for *VARS2* ($p = 0.0057$) (**Figure 5B**).

As expected, based on the increased steady-state RNA levels detected by RNA-seq data upon Dex stimulation, the number of cells with one or two nascent RNA signals for *ERRFI1*, *FKBP5*, and *VARS2* increased after Dex treatment for either 2 or 4 hours compared to untreated controls (**Supplementary Figure 5**). However, despite robust transcriptional induction, TAD boundary distances remained unchanged ($p > 0.3$ for all comparisons) (**Figure 5C**). The proportion of alleles within 250 nm also did not differ between Dex-treated and control conditions (Mann-Whitney U test, $p > 0.2$) (**Figure 5C**). Together, these results demonstrate that TAD boundary architecture is unaffected by acute transcriptional activation, reinforcing the notion that TAD structure and gene activity are uncoupled.

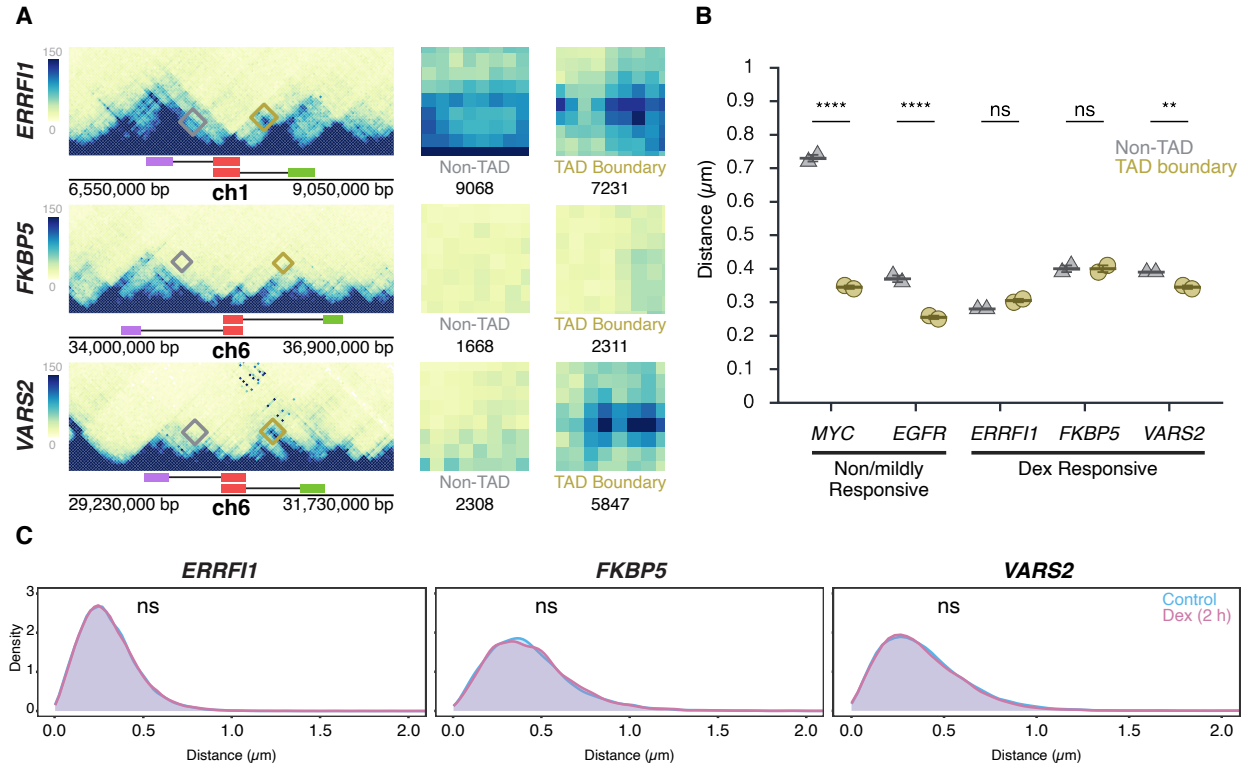

Figure 5. Transcription stimulation does not alter TAD boundary interactions

(A) *Micro-C maps for the ERRFI1, FKBP5, and VARS2 TADs and neighboring regions, showing TAD boundaries (green, red) and equidistant non-TAD control regions (purple) in HFF; corresponding probe positions are indicated. Interactions between the 5' TAD boundaries and the 3' TAD (yellow) or equidistant non-TAD control regions (grey) are highlighted, and total Micro-C contacts between regions are quantified, showing prominent contact frequency between ERRFI1, VARS2, and FKBP5 TAD boundaries, as well as the non-TAD region of ERRFI1.*

(B) *Comparison of TAD boundary and non-TAD region distances for EGFR, MYC, ERRFI1, FKBP5, and VARS2 in HBECs as measured by DNA HiFISH. Dot plots of the mean of median distances from two experiments (11,000 – 49,000 alleles per condition). Error bars represent SEM. Statistical significance was calculated using two-way ANOVA with Bonferroni correction: ****$p < 0.0001$; **$p < 0.01$; ns, not significant ($p \geq 0.05$).*

(C) *Measurement of boundary distances. Distance distributions of ERRFI1, FKBP5, and VARS2 TADs in untreated and 2-hour Dex-treated HBEC. Between 2,500 and 6,000 alleles were analyzed per condition. Values represent an individual dataset from a single*

experiment representative of multiple experiments. Mann-Whitney U test p-values are indicated as follows: ns, not significant (p ≥ 0.05).

TAD boundary architecture and gene expression

Our results indicate that gene expression status does not affect TAD boundary architecture. We next asked whether, conversely, alterations in TAD boundary structure affect transcription. To do so, we depleted the cohesin complex component RAD21 or the boundary protein CTCF in HCT116 cells using previously characterized auxin-inducible degron (AID) systems[18, 54, 55] and assessed the effect of depletion of either factor on boundary structure and transcription by DNA/RNA HiFISH (**Figure 6**; **Supplementary Figure 6A**).

Consistent with prior studies, treatment of HCT116-RAD21-AID cells with auxin for 3 or 6 hours resulted in near-complete degradation of RAD21[18, 54] (**Supplementary Figure 6A**). RAD21 depletion significantly increased the 5'-3' TAD boundary distances for both the *EGFR* and *MYC* TADs (**Figure 6A–B**). For *EGFR*, the median boundary distance increased from 0.25 ± 0.20 μm (control; median ± IQR) to 0.39 ± 0.36 μm (RAD21-depleted, Mann-Whitney U test, $p < 1\times10^{-10}$). For *MYC*, the median increased from 0.34 ± 0.26 μm to 0.49 ± 0.49 μm (U test, $p < 1\times10^{-10}$). The fraction of alleles with TAD boundaries within 250 nm decreased from 49% to 26% for *EGFR* and from 29% to 18% for *MYC* upon depletion of RAD21 (**Figure 6B**). RAD21 depletion also reduced the expression of *EGFR* and *MYC*, with the median number of transcription sites per cell decreasing by 1.6-fold and 2.1-fold, respectively (**Figure 6C**). In line with gene repression, the percentage of cells with no detectable nascent RNA signal increased for both *EGFR* and *MYC* (Bonferroni-adjusted p-values = 2.70e-3 and <0.0001, respectively) (**Figure 6C**), and monoallelic expression frequencies also modestly decreased (**Figure 6C**). Similar results were observed for the *ERRFI1 gene* upon loss of RAD21 (**Supplementary Figure 6B**).

The reduction in gene expression upon loss of RAD21 may either be due to changes in TAD architecture or due to local effects of RAD21, such as in enhancer-promoter interactions[19-21]. To more directly assess a possible role of TAD structure on gene

expression, we depleted the boundary factor CTCF as previously described[55] (**Supplementary Figure 6A**). Depletion of CTCF increased *MYC* TAD boundary distances (median increased from 0.33 ± 0.25 μm to 0.44 ± 0.30 μm; Mann-Whitney U test, $p < 1\times10^{-100}$). No change in *EGFR* TAD boundary distances was detected upon CTCF depletion, likely due to the smaller size of the *EGFR* TAD (U test, $p \geq 0.01$; **Figure 6C**, **Supplementary Figure 1**). Regardless, no significant differences were observed in the expression of *MYC* or *EGFR* following CTCF depletion (Bonferroni-adjusted p-value > 0.5; **Figure 6C**). A similar lack of an effect on gene expression was observed for the *ERRFI1* gene upon depletion of CTCF (**Supplementary Figure 6C**). Altogether, these results demonstrate that disruption of TAD boundary architecture is insufficient to alter gene expression.

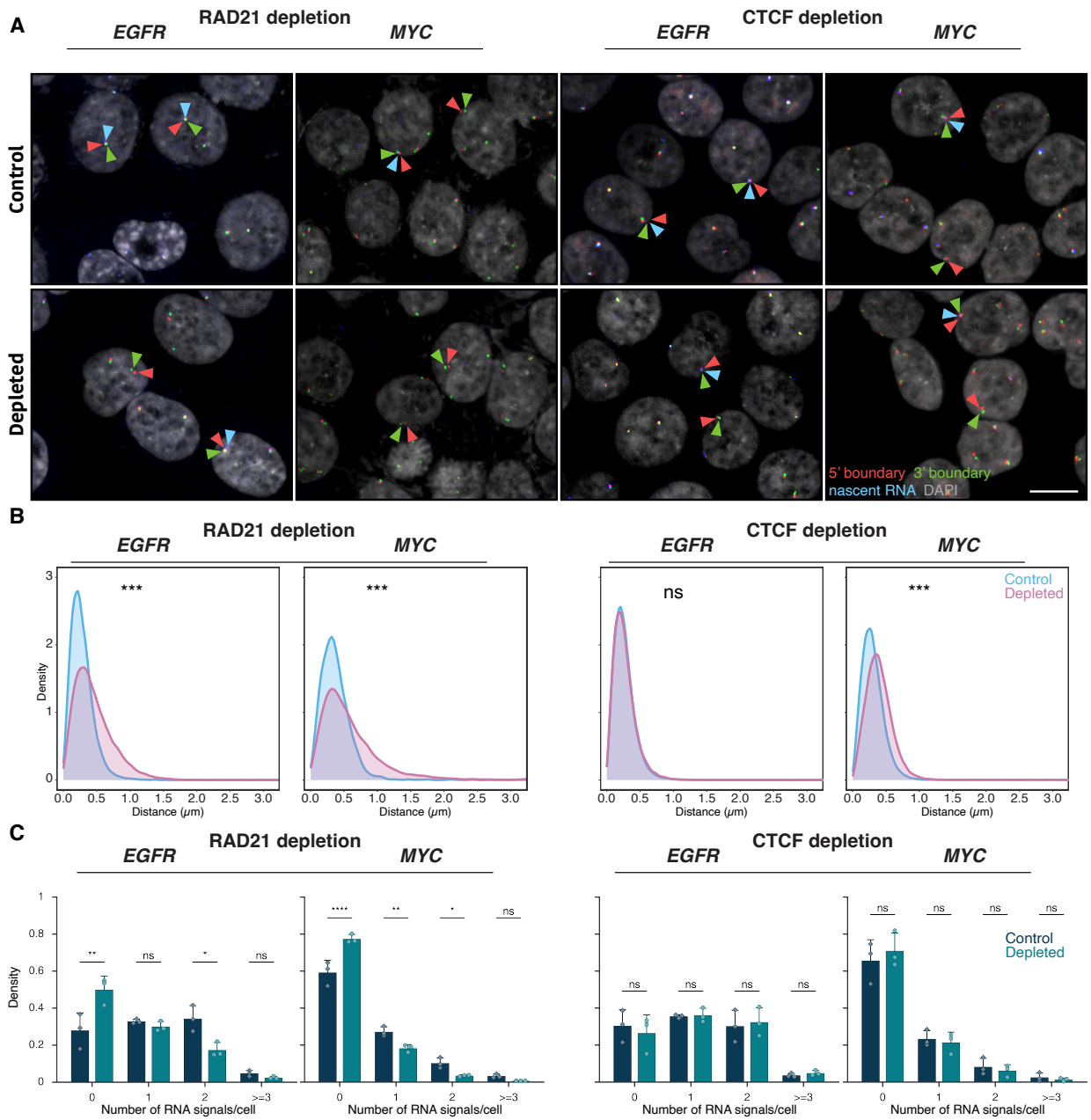

Figure 6. Effects of RAD21 and CTCF depletion on TAD boundary architecture and gene expression

(A) *Representative DNA/RNA HiFISH images of EGFR nascent RNA FISH (blue) and its 3' (green) and 5' (red) TAD boundaries DNA FISH in HCT116-RAD21-AID1 and HCT116-CTCF-AID2 cells, respectively, in control and auxin-treated conditions. Scale bar: 10 μm.* ***(B)*** *TAD boundary distances and non-TAD controls after RAD21 or CTCF depletion for 3 hours. Values represent an individual dataset from a single experiment representative of multiple experiments. Between 13,000 and 127,500 alleles were analyzed per condition.*

*Mann-Whitney U test p-values are indicated as follows: *** $p < 1\times10^{-100}$; ns, not significant ($p \geq 0.05$).*

(C) *Fraction of silent (0), monoallelic (1), biallelic (2), and triallelic or more (≥3) expression of the indicated genes in individual cells after 3 hours or no auxin treatment in HCT116-RAD21-AID1 or HCT116-CTCF-AID2 cells. At least 20,000 cells were measured per experiment. Data represent values from at least two independent experiments (diamonds and circles); diamonds (DMSO control) and circles (RAD21 or CTCF-depleted) represent the mean of means and error bars indicate SD. p-values from two-way ANOVA with Bonferroni correction are shown as: ****$p < 0.0001$; **$p < 0.01$; *$p < 0.05$; ns, not significant ($p \geq 0.05$).*

DISCUSSION

We have used high-throughput DNA/RNA FISH to directly and quantitatively probe the relationship of TAD structure to gene activity at the single-cell and -allele level. We find in various experimental settings that TAD boundary proximity is unrelated to gene activity. Our results suggest that TAD structure is largely uncoupled from transcription activity.

Uncoupling of TAD structure and gene activity is supported by several observations. TAD boundary distances were indistinguishable between transcriptionally active and inactive alleles across several loci and cell types, even when measured in the same cell nucleus. Furthermore, neither global transcription inhibition nor gene-specific induction of transcription altered TAD boundary architecture, suggesting that short-term transcription dynamics do not affect TAD boundary interactions. These results align with genome-wide findings from population-based studies indicating that global transcription inhibition does not disrupt TAD structure[18]. A lack of correlation between TAD structure and gene expression has also been noted in early *Drosophila* development, where TAD architecture is unrelated to cell-type-specific gene expression patterns[23, 24], and TADs form prior to the establishment of cell-type-specific gene expression programs[23, 24]. Furthermore, interference with intra-TAD connections and disrupting long-range inter-TAD loops at a large scale in *Drosophila* does not alter the expression of a majority of genes[22]. Furthermore, we find that loss of boundary structure by depletion of the architectural boundary protein CTCF did not cause changes in expression of *MYC* and *EGFR*. Combined, these findings suggest that TAD structure, or at least their boundaries, are largely decoupled from RNA Polymerase II activity.

These observations point to a model in which the precise demarcation of TAD boundaries by CTCF only plays a relatively minor role in determining the activity of the genes within the TAD. This interpretation is in line with recent ultra-resolution live-cell imaging, which revealed that at short genomic distances (< ~200 kb), chromatin loci encounter one another frequently due to spatial proximity alone, resulting in sub-minute search times largely independent of distance[56]. Beyond this range, encounter probability declines sharply, and cohesin becomes essential to dynamically bridge distal regulatory elements through active loop extrusion[56]. This extrusion-driven process enables long-range (> ~200 kb) interactions, particularly between enhancers and promoters, that are

genomically relatively rare and would otherwise be kinetically disfavored. Upon cohesin depletion, these rapid, distance-independent searches collapse into a diffusive regime, and the loss of encounter kinetics across TAD borders disappears, indicating that TAD boundaries act primarily as kinetic rather than structural barriers[56]. In support of this hypothesis, we find differential effects of loss of either RAD21or CTCF and genome-wide analyses have shown that boundary-proximal genes are more affected by cohesin depletion than those residing within the interior of TADs[57], reinforcing the notion that cohesin's role is most critical in bridging long-range separations across or adjacent to domain borders[58]. This view is consistent with our observation that cohesin depletion had a more pronounced effect at the *MYC* locus, which is associated with a super-enhancer, undergoes long-range enhancer regulation, and lies near a strong boundary within a large TAD, compared to the smaller *EGFR* TAD and loci positioned in more internal chromatin regions. In contrast, the role of CTCF appears primarily architectural - defining the domain limits that constrain extrusion.

Our findings argue against a strict regulatory role for TAD boundaries in controlling gene expression. Rather than acting as stringent regulators of gene expression, TADs appear to serve primarily to organize chromatin topology at a global scale[59]. Our results suggest that transcriptional regulation occurs primarily at finer scales of genome organization - such as enhancer-promoter loops or sub-TAD structures - rather than being governed by the overall configuration of an entire TAD. This interpretation is consistent with our findings that the overall TAD structure is not sensitive to the transcriptional status of its genes, and with observations by others demonstrating local, intra-TAD effects, of transcription on chromatin structure[37, 38]. Interestingly, effects of transcription on TAD structure have been observed during thymocyte differentiation[36]. Notably, the affected genes were located near their TAD boundaries, further pointing to local effects of gene activity on chromatin structure. These transcriptional effects may be due to competition between transcription and cohesin-mediated loop extrusion, as demonstrated by live cell imaging for Sox2, which showed that transcribing RNA polymerase II disrupts cohesin's ability to extrude local loops, while strong local loop extrusion can, in turn, hinder transcription[27]. The complex interplay of gene expression, local chromatin organization, and TAD structure is further highlighted by the observation of distinct, and only partially

overlapping, effects on gene expression upon loss of either of the two cohesin regulators WAPL and NIPBL[60]. Taken together, these findings indicate that transcriptional regulation operates at finer spatial and temporal scales than the overall TAD conformation and that global genome organization at the level of TADs functions more as a general structural framework rather than a fixed regulatory architecture.

Our observations are limited to the relationship of transcription and TAD boundaries rather than the TAD as a whole. Boundaries may move without affecting the internal compaction or regulatory organization of the domain, and conversely, the internal structure may change while the boundary distance remains constant. This behavior is in line with the dynamic properties of TADs observed in living cells and highlights the variability of TAD structure at the single allele level[31, 32]. The fluidity of TAD structure aligns well with the notion that the function of TADs is not to act as strict, binary regulators of gene expression, but rather that TADs facilitate chromatin interactions, thus exerting a modifying rather than deterministic role in gene expression[59]. Future work that maps internal domain contacts in single cells in parallel with transcriptional state should provide deeper insight into the relationship between TAD chromatin and transcription.

Regardless, our observations support the view that the structural and transcriptional layers of genome organization can be partially uncoupled. These insights have implications for interpreting chromatin conformation maps and for understanding the scale at which genome architecture influences transcriptional regulation.

MATERIALS AND METHODS

Cell culture

Human bronchial epithelial cells (HBEC3-KT; HBEC) are derived from normal human bronchial tissue and immortalized by stable transduction with hTERT and CDK4(61). HBEC3-KT cells were maintained in keratinocyte serum-free medium (Thermo Fisher Scientific, cat. no. 17005042) supplemented with bovine pituitary extract (Thermo Fisher Scientific, cat. no. 13028014), human growth hormone (Thermo Fisher Scientific, cat. no. 1045013), and 50 U/ml penicillin/streptomycin (Thermo Fisher Scientific, cat. no. 15070063). HBEC-*MYC*-MS2, a derivative of HBEC with 12xMS2 inserted at the 3′ end of *MYC* on both alleles, constitutively expressing a GFP-MS2 coat protein fusion, was maintained under the same conditions.

Human foreskin fibroblasts (HFF), immortalized with hTERT[62], were cultured in DMEM (Thermo Fisher Scientific, cat. no. 10569010) with 10% fetal bovine serum (Thermo Fisher Scientific, cat. no. 10082147) and penicillin/streptomycin. HCT-116 RAD21-mAID-mClover (RAD21-mAC) cells[54] were cultured in McCoy's 5A medium (Thermo Fisher Scientific) with 10% FBS, 2 mM L-glutamine, and 100 U/ml penicillin, and 100 µg/ml streptomycin (Thermo Fisher Scientific, cat. no. 15070063). All cells were grown at 37°C in 5% CO_2 and split 1:4 twice weekly. Cells were seeded into 384-well imaging plates (PhenoPlate, Revvity, cat. no. 6057500) and allowed to grow to ~80% confluency prior to experiments[63].

Cell treatments

For transcription inhibition, HBEC and HFF cells were treated with 100 µM DRB (Sigma-Aldrich, cat. no. D1916) in culture medium for 2 hours, then fixed as described below. For glucocorticoid-mediated transcriptional stimulation, HBEC cells were cultured in Airway Epithelial Cell Basal Medium (ATCC, cat. no. PCS-300-030) supplemented with the Bronchial Epithelial Cell Growth Kit (ATCC, cat. no. PCS-300-040) and penicillin/streptomycin. To eliminate background glucocorticoid activity, cells were transferred 24 hours before induction to hormone-free medium, prepared by supplementing the basal ATCC Airway Epithelial Medium with HLL Supplement, L-glutamine, and penicillin/streptomycin while omitting both the P-extract and the Airway

Epithelial Cell Supplement, as these components contain glucocorticoids. Dexamethasone (Dex; Sigma-Aldrich, cat. no. D4902) was prepared as a 100 μM stock solution in ethanol, aliquoted, protected from light, and stored at –20 °C. For induction, HBEC cells were treated with 100 nM Dex (final concentration) for 2 or 4 hours. For RAD21 depletion, HCT116-RAD21-AID1 cells were treated with 0.17 μM auxin (Sigma-Aldrich, cat. no. I3750) or DMSO vehicle control for 3 hours[18, 54]. Cells were fixed with 4% PFA (Electron Microscopy Sciences, cat. no. 15710) in PBS (Millipore Sigma, cat. no. D8537) for 10 minutes, washed, and stored in PBS at 4°C. For CTCF depletion, HCT116-CTCF-AID2 cells were treated with 1 μM 5-Ph-IAA (GLPBio, cat. no. GC46061) or DMSO vehicle control in McCoy's 5A medium (Thermo Fisher Scientific, cat. no. 16600082) supplemented with charcoal-stripped fetal bovine serum[55] (R&D Systems, cat. no. S11650H). The 5-Ph-IAA (AID2 ligand) working solution was freshly prepared from a 1 mM intermediate stock immediately before use. Cells were cultured for approximately 36 hours to reach 80–90% confluence before treatment. The medium was then replaced with an equal volume of medium containing 1 μM 5-Ph-IAA or an equivalent volume of DMSO control, and cells were incubated for 3 hours at 37°C. Following treatment, cells were directly fixed without washing in 4% paraformaldehyde (Electron Microscopy Sciences, cat. no. 15710) in PBS (Millipore Sigma, cat. no. D8537) for 10 minutes, washed, and stored in PBS at 4 °C until further processing.

FISH probes

BAC probes targeting *MYC* or *EGFR* TAD boundaries (RP11-765K23, RP11-717D13 for *MYC*; RP11-366D3, RP11-98C17 for *EGFR*) were obtained from the BACPAC Resources Center (BACPAC Resources Center). Negative controls targeting equidistant upstream regions were RP11-788I22 and RP11-112A3 (See Supplementary Table S1 for a complete list of BAC probes). BAC probes were labeled by nick translation at 14°C for 80 minutes using DY549P1-dUTP or DY488-dUTP (Dyomics) as previously described[63]. Labeled probes were ethanol-precipitated with 38 ng/μl Cot-1 DNA (Millipore Sigma), 256 ng/μl yeast tRNA, and 0.1 M sodium acetate, washed, and resuspended in hybridization buffer which is made up of 30% formamide (pH 7.0), 10% dextran sulfate, 0.5% Tween-20, 2× SSC, 0.5× RNAsecure™ RNAse inhibitor, and 3% THE RNA Storage Solution (Thermo Fisher Scientific, cat. No. AM7001) dissolved entirely in molecular - H2O.

Stellaris® RNA probes (LGC Biosearch Technologies) targeting intron one of *MYC* and *EGFR* consisted of 48 20-mer oligonucleotides labeled with Atto647N (see Supplementary Figure 2 for details).

DNA/RNA HiFISH in 384-well plates

hiFISH was performed as described[39]. In brief, cells were permeabilized in 0.5% saponin/0.5% Triton X-100/1× RNAsecure™ in PBS for 20 minutes, deproteinated in 0.1 N HCl for 15 minutes, neutralized in 2× SSC, and equilibrated in 50% formamide/2× SSC overnight at 4°C. Hybridization mixtures (0.4 µg DNA probe + 12.5 µM RNA probe + hybridization buffer) were denatured at 85°C for 7 minutes and applied to cells, followed by 48-hour incubation at 37°C. Post-hybridization washes included 50% formamide/2× SSC at 37°C (2 × 1 hour), 2× SSC (twice), and prewarmed 1× SSC and 0.1× SSC at 45°C (three washes each). Nuclei were stained with 3 µg/ml of 4′,6-diamidino-2-phenylindole (DAPI) in 2× SSC.

High-throughput image acquisition

Images were acquired using a Yokogawa CV8000 spinning-disk confocal microscope as described in[39] with a 60× water objective (NA 1.2), four laser lines (405, 488, 561, 640 nm), and appropriate emission filters. Z-stacks spanning 7 µm (1 µm steps) were collected in four channels.

Image pre-processing

For simultaneous FISH, images were analyzed directly. For sequential FISH, DNA and RNA images were registered as described[39] using cross-correlation algorithms implemented in Python 3.8 to align DAPI signals (GitHub: https://github.com/CBIIT/DNA_RNA_registration).

High-throughput image analysis

HiTIPS software[40] was used for segmentation and detection of FISH signals. Nucleus segmentation used CellPose [64], and segmentation parameters were adjusted per plate, with quality-control overlays to confirm accuracy. Data from each well were consolidated into experiment-wide datasets in R (R Core Team, 2024) using tidyverse[65] and other

packages[66, 67]. For diploid cells, only cells with two DNA signals and ≤2 RNA signals were included for analysis. For analysis of triploid *MYC* HCT116, only cells with two and three *MYC* DNA signals and ≤3 RNA signals were included for analysis. TAD boundary pairs were identified as closest neighbors of a 5' and 3' signal. An active allele was defined based on the presence of an RNA signal within 1 μm of either boundary signal, based on analysis of RNA-DNA distances in pilot experiments demonstrating that >95% RNA signals were located within 1 μm.

Micro-C analysis

Published Micro-C XL data from H1-hESC and HFFc6 cells[42] were visualized using UCSC Genome Browser[68] and 4DN Data Portal[69, 70]. Heatmaps were displayed with UCSC Track Settings: Display mode Full, Score Maximum Auto-scale, Draw mode triangle, Color HEX (#000000), and no interaction distance filter.

ChromHMM analysis

Chromatin state annotation for the HCT116 cell line was obtained from ENCODE (file accession ENCFF993RQV, annotation ID ENCSR448SWW, hg38) using the ChromHMM algorithm[44]. Each genomic interval was assigned to one of 15 functional states ENCODE Project Consortium, 2020).

Data analysis

Distance calculations were performed in R using SpatialTools[71]. Statistical comparisons used Kolmogorov–Smirnov[72], Wilcoxon rank-sum[73], and Dunn's test with Bonferroni correction[74, 75]. p-values were categorized as *** $p < 0.001$, ** $p < 0.01$, * $p < 0.05$, ns $p \geq 0.05$.

Statistical tests

KS tests compared distributions of radial distances; Wilcoxon tests compared medians of two groups; Dunn's test followed Kruskal-Wallis ANOVA for multi-group comparisons[76]. Statistical thresholds and exact p-values are reported in figure legends.

DATA AVAILABILITY

Code for DNA/RNA image registration is available at https://github.com/CBIIT/DNA_RNA_registration[39]. The HiTIPS source code is available

at https://github.com/CBIIT/HiTIPS, with full documentation—including package structure, functions, installation instructions, user guidance, output table descriptions, and developer resources—accessible at https://hitips.readthedocs.io/en/latest/[40]. All R scripts used for image quantification, including calculations of TAD boundary distances and single-cell gene-expression measurements from DNA/RNA HiFISH data, are publicly available at https://github.com/CBIIT/mistelilab-tad-ge. Uncropped ImageJ-generated TIFF composites underlying the microscopy panels, along with the DNA/RNA HiFISH datasets used in this study, have been deposited in Figshare (DOI: 10.6084/m9.figshare.30728354).

ACKNOWLEDGEMENTS

We thank members of the Misteli lab for input throughout the study. RNAseq data was kindly provided by Thomas Johnson, NCI. Computation was performed on the NIH HPC Biowulf cluster. F.A. was supported by a graduate fellowship from the Ministry of Education of Saudi Arabia. This research was supported by the Intramural Research Program of the National Institutes of Health (NIH), National Cancer Institute NCI, Center for Cancer Research through grant 1-ZIA-BC010309 to T.M., grant 1-ZIC-BC-011567 to HiTIF, and grant 1-ZIA-BC-011383 to D. L. The contributions of the NIH author(s) were made as part of their official duties as NIH federal employees, are in compliance with agency policy requirements, and are considered Works of the United States Government. However, the findings and conclusions presented in this paper are those of the author(s) and do not necessarily reflect the views of the NIH or the U.S. Department of Health and Human Services.

CONFLICT OF INTEREST

The authors declare no conflicts of interest.

REFERENCES

1. Misteli T. 2020. The Self-Organizing Genome: Principles of Genome Architecture and Function. Cell. 183: 28–45. doi:10.1016/j.cell.2020.09.014.

2. Dixon J. R., Selvaraj S., Yue F., Kim A., Li Y., Shen Y., et al. 2012. Topological domains in mammalian genomes identified by analysis of chromatin interactions. Nature. 485: 376–80. doi:10.1038/nature11082.

3. Lieberman-Aiden E., Van Berkum N. L., Williams L., Imakaev M., Ragoczy T., Telling A., et al. 2009. Comprehensive mapping of long-range interactions reveals folding principles of the human genome. Science. 326: 289–93. doi:10.1126/science.1181369.

4. Nora E. P., Lajoie B. R., Schulz E. G., Giorgetti L., Okamoto I., Servant N., et al. 2012. Spatial partitioning of the regulatory landscape of the X-inactivation centre. Nature. 485: 381–5. doi:10.1038/nature11049.

5. Sexton T., Yaffe E., Kenigsberg E., Bantignies F., Leblanc B., Hoichman M., et al. 2012. Three-dimensional folding and functional organization principles of the Drosophila genome. Cell. 148: 458–72. doi:10.1016/j.cell.2012.01.010.

6. Dekker J., Mirny L. 2016. The 3D Genome as Moderator of Chromosomal Communication. Cell. 164: 1110–21. doi:10.1016/j.cell.2016.02.007.

7. Rowley M. J., Corces V. G. 2018. Organizational principles of 3D genome architecture. Nat Rev Genet. 19: 789–800. doi:10.1038/s41576-018-0060-8.

8. Fudenberg G., Imakaev M., Lu C., Goloborodko A., Abdennur N., Mirny L. A. 2016. Formation of Chromosomal Domains by Loop Extrusion. Cell Rep. 15: 2038–49. doi:10.1016/j.celrep.2016.04.085.

9. Bell A. C., West A. G., Felsenfeld G. 1999. The protein CTCF is required for the enhancer blocking activity of vertebrate insulators. Cell. 98: 387–96. doi:10.1016/s0092-8674(00)81967-4.

10. Hark A. T., Schoenherr C. J., Katz D. J., Ingram R. S., Levorse J. M., Tilghman S. M. 2000. CTCF mediates methylation-sensitive enhancer-blocking activity at the H19/Igf2 locus. Nature. 405: 486–9. doi:10.1038/35013106.

11. Chakraborty S., Wenzlitschke N., Anderson M. J., Eraso A., Baudic M., Thompson J. J., et al. 2025. Deletion of a single CTCF motif at the boundary of a chromatin domain with three FGF genes disrupts gene expression and embryonic development. Dev Cell. 60: 1838–53 e9. doi:10.1016/j.devcel.2025.02.002.

12. Franke M., Ibrahim D. M., Andrey G., Schwarzer W., Heinrich V., Schopflin R., et al. 2016. Formation of new chromatin domains determines pathogenicity of genomic duplications. Nature. 538: 265–9. doi:10.1038/nature19800.

13. Lupianez D. G., Kraft K., Heinrich V., Krawitz P., Brancati F., Klopocki E., et al. 2015. Disruptions of topological chromatin domains cause pathogenic rewiring of gene-enhancer interactions. Cell. 161: 1012–25. doi:10.1016/j.cell.2015.04.004.

14. Mateo L. J., Murphy S. E., Hafner A., Cinquini I. S., Walker C. A., Boettiger A. N. 2019. Visualizing DNA folding and RNA in embryos at single-cell resolution. Nature. 568: 49–54. doi:10.1038/s41586-019-1035-4.

15. Spielmann M., Lupianez D. G., Mundlos S. 2018. Structural variation in the 3D genome. Nat Rev Genet. 19: 453–67. doi:10.1038/s41576-018-0007-0.

16. Dorsett D., Krantz I. D. 2009. On the molecular etiology of Cornelia de Lange syndrome. Ann N Y Acad Sci. 1151: 22–37. doi:10.1111/j.1749-6632.2008.03450.x.

17. Nora E. P., Goloborodko A., Valton A. L., Gibcus J. H., Uebersohn A., Abdennur N., et al. 2017. Targeted Degradation of CTCF Decouples Local Insulation of Chromosome Domains from Genomic Compartmentalization. Cell. 169: 930–44 e22. doi:10.1016/j.cell.2017.05.004.

18. Rao S. S. P., Huang S. C., Glenn St Hilaire B., Engreitz J. M., Perez E. M., Kieffer-Kwon K. R., et al. 2017. Cohesin Loss Eliminates All Loop Domains. Cell. 171: 305–20 e24. doi:10.1016/j.cell.2017.09.026.

19. Kagey M. H., Newman J. J., Bilodeau S., Zhan Y., Orlando D. A., Van Berkum N. L., et al. 2010. Mediator and cohesin connect gene expression and chromatin architecture. Nature. 467: 430–5. doi:10.1038/nature09380.

20. Merkenschlager M., Odom D. T. 2013. CTCF and cohesin: linking gene regulatory elements with their targets. Cell. 152: 1285–97. doi:10.1016/j.cell.2013.02.029.

21. Phillips-Cremins J. E., Sauria M. E., Sanyal A., Gerasimova T. I., Lajoie B. R., Bell J. S., et al. 2013. Architectural protein subclasses shape 3D organization of genomes during lineage commitment. Cell. 153: 1281–95. doi:10.1016/j.cell.2013.04.053.

22. Ghavi-Helm Y., Jankowski A., Meiers S., Viales R. R., Korbel J. O., Furlong E. E. M. 2019. Highly rearranged chromosomes reveal uncoupling between genome topology and gene expression. Nat Genet. 51: 1272–82. doi:10.1038/s41588-019-0462-3.

23. Espinola S. M., Gotz M., Bellec M., Messina O., Fiche J. B., Houbron C., et al. 2021. Cis-regulatory chromatin loops arise before TADs and gene activation, and are independent of cell fate during early Drosophila development. Nat Genet. 53: 477–86. doi:10.1038/s41588-021-00816-z.

24. Ing-Simmons E., Vaid R., Bing X. Y., Levine M., Mannervik M., Vaquerizas J. M. 2021. Independence of chromatin conformation and gene regulation during Drosophila dorsoventral patterning. Nat Genet. 53: 487–99. doi:10.1038/s41588-021-00799-x.

25. Chakraborty S., Kopitchinski N., Zuo Z., Eraso A., Awasthi P., Chari R., et al. 2023. Enhancer-promoter interactions can bypass CTCF-mediated boundaries and contribute to phenotypic robustness. Nat Genet. 55: 280–90. doi:10.1038/s41588-022-01295-6.

26. Hsieh T. S., Cattoglio C., Slobodyanyuk E., Hansen A. S., Darzacq X., Tjian R. 2022. Enhancer-promoter interactions and transcription are largely maintained upon acute loss of CTCF, cohesin, WAPL or YY1. Nat Genet. 54: 1919–32. doi:10.1038/s41588-022-01223-8.

27. Platania A., Erb C., Barbieri M., Molcrette B., Grandgirard E., De Kort M. A. C., et al. 2024. Transcription processes compete with loop extrusion to homogenize promoter and enhancer dynamics. Sci Adv. 10: eadq0987. doi:10.1126/sciadv.adq0987.

28. Taylor T., Sikorska N., Shchuka V. M., Chahar S., Ji C., Macpherson N. N., et al. 2022. Transcriptional regulation and chromatin architecture maintenance are decoupled functions at the Sox2 locus. Genes Dev. 36: 699–717. doi:10.1101/gad.349489.122.

29. Bintu B., Mateo L. J., Su J. H., Sinnott-Armstrong N. A., Parker M., Kinrot S., et al. 2018. Super-resolution chromatin tracing reveals domains and cooperative interactions in single cells. Science. 362. doi:10.1126/science.aau1783.

30. Cattoni D. I., Cardozo Gizzi A. M., Georgieva M., Di Stefano M., Valeri A., Chamousset D., et al. 2017. Single-cell absolute contact probability detection reveals chromosomes are organized by multiple low-frequency yet specific interactions. Nat Commun. 8: 1753. doi:10.1038/s41467-017-01962-x.

31. Finn E. H., Pegoraro G., Brandao H. B., Valton A. L., Oomen M. E., Dekker J., et al. 2019. Extensive Heterogeneity and Intrinsic Variation in Spatial Genome Organization. Cell. 176: 1502–15 e10. doi:10.1016/j.cell.2019.01.020.

32. Gabriele M., Brandao H. B., Grosse-Holz S., Jha A., Dailey G. M., Cattoglio C., et al. 2022. Dynamics of CTCF- and cohesin-mediated chromatin looping revealed by live-cell imaging. Science. 376: 496–501. doi:10.1126/science.abn6583.

33. Sabate T., Lelandais B., Bertrand E., Zimmer C. 2023. Polymer simulations guide the detection and quantification of chromatin loop extrusion by imaging. Nucleic Acids Res. 51: 2614–32. doi:10.1093/nar/gkad034.

34. Rodriguez J., Ren G., Day C. R., Zhao K., Chow C. C., Larson D. R. 2019. Intrinsic Dynamics of a Human Gene Reveal the Basis of Expression Heterogeneity. Cell. 176: 213–26 e18. doi:10.1016/j.cell.2018.11.026.

35. Sood V., Holewinski R., Andresson T., Larson D. R., Misteli T. 2025. Identification of molecular determinants of gene-specific bursting patterns by high-throughput imaging screens. Mol Cell. 85: 913–28 e8. doi:10.1016/j.molcel.2025.01.022.

36. Chahar S., Ben Zouari Y., Salari H., Kobi D., Maroquenne M., Erb C., et al. 2023. Transcription induces context-dependent remodeling of chromatin architecture during differentiation. PLoS Biol. 21: e3002424. doi:10.1371/journal.pbio.3002424.

37. Luppino J. M., Field A., Nguyen S. C., Park D. S., Shah P. P., Abdill R. J., et al. 2022. Co-depletion of NIPBL and WAPL balance cohesin activity to correct gene misexpression. PLoS Genet. 18: e1010528. doi:10.1371/journal.pgen.1010528.

38. Shaban H. A., Friman E. T., Deluz C., Tollenaere A., Katanayeva N., Suter D. M. 2024. Individual transcription factors modulate both the micromovement of chromatin and its long-range structure. Proc Natl Acad Sci U S A. 121: e2311374121. doi:10.1073/pnas.2311374121.

39. Almansour F., Keikhosravi A., Pegoraro G., Misteli T. 2024. Allele-level visualization of transcription and chromatin by high-throughput imaging. Histochem Cell Biol. 162: 65–77. doi:10.1007/s00418-024-02289-7.

40. Keikhosravi A., Almansour F., Bohrer C. H., Fursova N. A., Guin K., Sood V., et al. 2024. High-throughput image processing software for the study of nuclear architecture and gene expression. Sci Rep. 14: 18426. doi:10.1038/s41598-024-66600-1.

41. Finn E. H., Pegoraro G., Shachar S., Misteli T. 2017. Comparative analysis of 2D and 3D distance measurements to study spatial genome organization. Methods. 123: 47–55. doi:10.1016/j.ymeth.2017.01.007.

42. Krietenstein N., Abraham S., Venev S. V., Abdennur N., Gibcus J., Hsieh T. S., et al. 2020. Ultrastructural Details of Mammalian Chromosome Architecture. Mol Cell. 78: 554–65 e7. doi:10.1016/j.molcel.2020.03.003.

43. Akgol Oksuz B., Yang L., Abraham S., Venev S. V., Krietenstein N., Parsi K. M., et al. 2021. Systematic evaluation of chromosome conformation capture assays. Nat Methods. 18: 1046–55. doi:10.1038/s41592-021-01248-7.

44. Ernst J., Kellis M. 2012. ChromHMM: automating chromatin-state discovery and characterization. Nat Methods. 9: 215–6. doi:10.1038/nmeth.1906.

45. Carstens S., Nilges M., Habeck M. 2016. Inferential Structure Determination of Chromosomes from Single-Cell Hi-C Data. PLoS Comput Biol. 12: e1005292. doi:10.1371/journal.pcbi.1005292.

46. Flyamer I. M., Gassler J., Imakaev M., Brandao H. B., Ulianov S. V., Abdennur N., et al. 2017. Single-nucleus Hi-C reveals unique chromatin reorganization at oocyte-to-zygote transition. Nature. 544: 110–4. doi:10.1038/nature21711.

47. Giorgetti L., Galupa R., Nora E. P., Piolot T., Lam F., Dekker J., et al. 2014. Predictive polymer modeling reveals coupled fluctuations in chromosome conformation and transcription. Cell. 157: 950–63. doi:10.1016/j.cell.2014.03.025.

48. Nagano T., Lubling Y., Stevens T. J., Schoenfelder S., Yaffe E., Dean W., et al. 2013. Single-cell Hi-C reveals cell-to-cell variability in chromosome structure. Nature. 502: 59–64. doi:10.1038/nature12593.

49. Stevens T. J., Lando D., Basu S., Atkinson L. P., Cao Y., Lee S. F., et al. 2017. 3D structures of individual mammalian genomes studied by single-cell Hi-C. Nature. 544: 59–64. doi:10.1038/nature21429.

50. Szabo Q., Jost D., Chang J. M., Cattoni D. I., Papadopoulos G. L., Bonev B., et al. 2018. TADs are 3D structural units of higher-order chromosome organization in Drosophila. Sci Adv. 4: eaar8082. doi:10.1126/sciadv.aar8082.

51. Baumli S., Endicott J. A., Johnson L. N. 2010. Halogen bonds form the basis for selective P-TEFb inhibition by DRB. Chem Biol. 17: 931–6. doi:10.1016/j.chembiol.2010.07.012.

52. Rahl P. B., Lin C. Y., Seila A. C., Flynn R. A., Mccuine S., Burge C. B., et al. 2010. c-Myc regulates transcriptional pause release. Cell. 141: 432–45. doi:10.1016/j.cell.2010.03.030.

53. Bothe M., Buschow R., Meijsing S. H. 2021. Glucocorticoid signaling induces transcriptional memory and universally reversible chromatin changes. Life Sci Alliance. 4. doi:10.26508/lsa.202101080.

54. Natsume T., Kiyomitsu T., Saga Y., Kanemaki M. T. 2016. Rapid Protein Depletion in Human Cells by Auxin-Inducible Degron Tagging with Short Homology Donors. Cell Rep. 15: 210–8. doi:10.1016/j.celrep.2016.03.001.

55. Yesbolatova A., Saito Y., Kitamoto N., Makino-Itou H., Ajima R., Nakano R., et al. 2020. The auxin-inducible degron 2 technology provides sharp degradation control in yeast, mammalian cells, and mice. Nat Commun. 11: 5701. doi:10.1038/s41467-020-19532-z.

56. Lee J., Chen L. F., Gaudin S., Gupta K., Novacic A., Spakowitz A., et al. 2025. Kinetic organization of the genome revealed by ultraresolution multiscale live imaging. Science. 389: eadx2202. doi:10.1126/science.adx2202.

57. Luppino J. M., Park D. S., Nguyen S. C., Lan Y., Xu Z., Yunker R., et al. 2020. Cohesin promotes stochastic domain intermingling to ensure proper regulation of boundary-proximal genes. Nat Genet. 52: 840–8. doi:10.1038/s41588-020-0647-9.

58. Tjalsma S. J. D., Rinzema N. J., Verstegen Mjam, Robers M. J., Nieto-Aliseda A., Gremmen R. A., et al. 2025. Long-range enhancer-controlled genes are hypersensitive to regulatory factor perturbations. Cell Genom. 5: 100778. doi:10.1016/j.xgen.2025.100778.

59. Misteli T., Finn E. H. 2021. Chromatin architecture is a flexible foundation for gene expression. Nat Genet. 53: 426–7. doi:10.1038/s41588-021-00813-2.

60. Schuijers J., Manteiga J. C., Weintraub A. S., Day D. S., Zamudio A. V., Hnisz D., et al. 2018. Transcriptional Dysregulation of MYC Reveals Common Enhancer-Docking Mechanism. Cell Rep. 23: 349–60. doi:10.1016/j.celrep.2018.03.056.

61. Ramirez R. D., Sheridan S., Girard L., Sato M., Kim Y., Pollack J., et al. 2004. Immortalization of human bronchial epithelial cells in the absence of viral oncoproteins. Cancer Res. 64: 9027–34. doi:10.1158/0008-5472.CAN-04-3703.

62. Benanti J. A., Galloway D. A. 2004. Normal human fibroblasts are resistant to RAS-induced senescence. Mol Cell Biol. 24: 2842–52. doi:10.1128/MCB.24.7.2842-2852.2004.

63. Finn E. H., Misteli T. 2021. A high-throughput DNA FISH protocol to visualize genome regions in human cells. STAR Protoc. 2: 100741. doi:10.1016/j.xpro.2021.100741.

64. Stringer C., Wang T., Michaelos M., Pachitariu M. 2021. Cellpose: a generalist algorithm for cellular segmentation. Nat Methods. 18: 100–6. doi:10.1038/s41592-020-01018-x.

65. Wickham Hadley; Averick, Mara; Bryan, Jennifer; Chang, Winston; Mcgowan, Lucy D.; François, Romain; Grolemund, Garrett; Hayes, Alex; Henry, Lionel; Hester, Jim; Kuhn, Max; Pedersen, Thomas Lin; Miller, Evan; Bache, Stefan M.; Müller, Kirill; Ooms, Jeroen; Robinson, David; Seidel, Dana; Spinu, Vitalie; Takahashi, Kohske; Vaughan, Davis; Wilke, Claus O.; Woo, Kara; Yutani, Hiroaki. 2019. Welcome to the tidyverse. Journal of Open Source Software. 4: 1686. doi:10.21105/joss.01686.

66. Author. 2024. R Packages by Malcolm Barrett program]. Comprehensive R Archive Network (CRAN). Available from: https://malcolmbarrett.r-universe.dev. Accessed Month Day, 2024.

67. Author. 2023. R Packages by Jim Hester program]. Comprehensive R Archive Network (CRAN). Available from: https://jimhester.r-universe.dev. Accessed Month Day, 2023.

68. Nassar L. R., Barber G. P., Benet-Pages A., Casper J., Clawson H., Diekhans M., et al. 2023. The UCSC Genome Browser database: 2023 update. Nucleic Acids Res. 51: D1188–D95. doi:10.1093/nar/gkac1072.

69. Dekker J., Belmont A. S., Guttman M., Leshyk V. O., Lis J. T., Lomvardas S., et al. 2017. The 4D nucleome project. Nature. 549: 219–26. doi:10.1038/nature23884.

70. Reiff S. B., Schroeder A. J., Kirli K., Cosolo A., Bakker C., Mercado L., et al. 2022. The 4D Nucleome Data Portal as a resource for searching and visualizing curated nucleomics data. Nat Commun. 13: 2365. doi:10.1038/s41467-022-29697-4.

71. Author. 2023. SpatialTools: R Functions for Spatial Statistics program]. 1.0. Comprehensive R Archive Network (CRAN). Available from: https://CRAN.R-project.org/package=SpatialTools. Accessed Month Day, 2023.

72. Massey F. J. 1951. The Kolmogorov–Smirnov Test for Goodness of Fit. Journal of the American Statistical Association. 46: 68–78. doi:10.1080/01621459.1951.10500769.

73. Wilcoxon F. 1945. Individual Comparisons by Ranking Methods. Biometrics Bulletin. 1: 80–3. doi:10.2307/3001968.

74. Dunn O. J. 1964. Multiple comparisons using rank sums. Technometrics. 6: 241–52. doi:10.1080/00401706.1964.10490181.

75. Shaffer J. P. 1995. Multiple Hypothesis Testing. Annual Review of Psychology. 46: 561–84. doi:10.1146/annurev.ps.46.020195.003021.

76. Kruskal W. H.; Wallis, W. A. 1952. Use of Ranks in One-Criterion Variance Analysis. Journal of the American Statistical Association. 47: 583–621. doi:10.1080/01621459.1952.10483441.

SUPPLEMENTARY INFORMATION

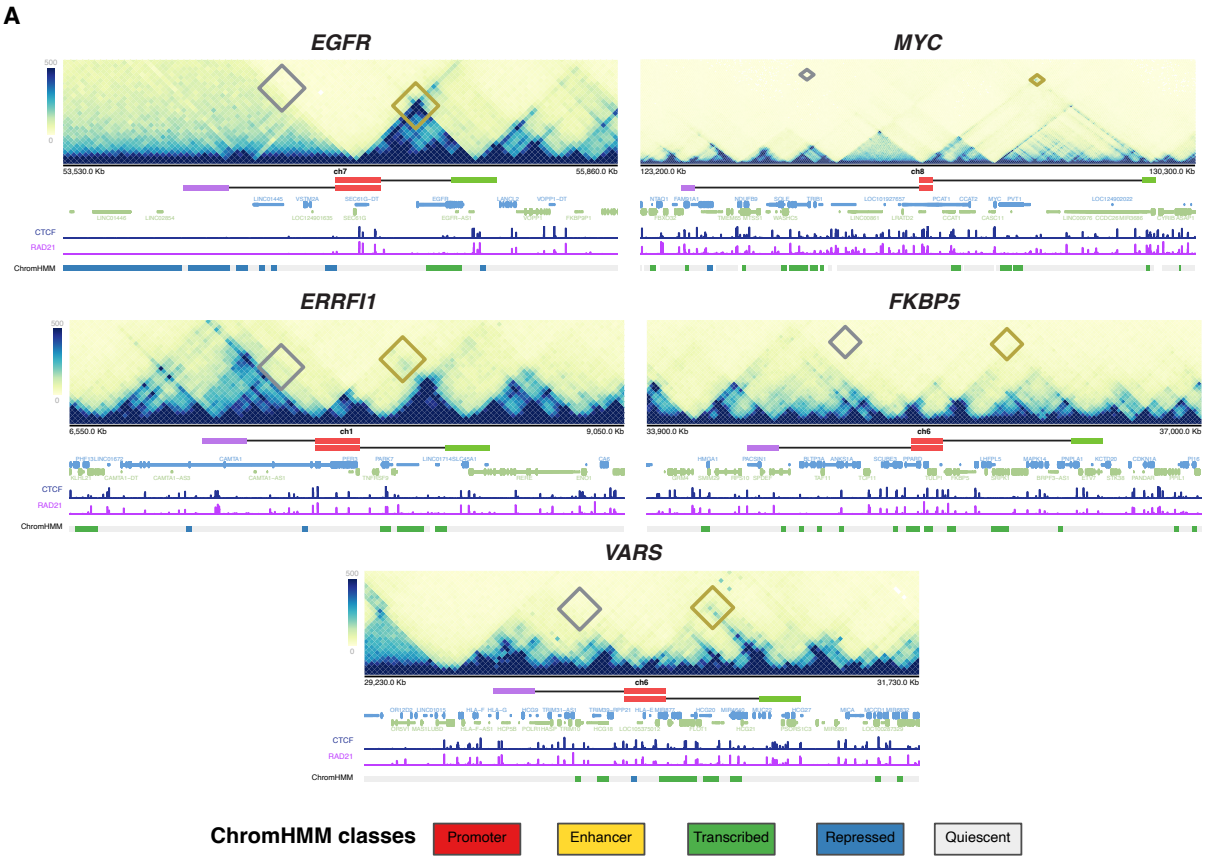

Supplementary Figure 1 Micro-C chromosome interaction maps and ChromHMM analysis of *EGFR*, *MYC*, *ERRFI1*, *FKBP5*, and *VARS2* TADs in HFFc6

ChromHMM chromatin states for two different foreskin fibroblast cell lines. The cytogenic chromosome band track (grey) indicates the chromosome location of the indicated loci. The gene reference track (blue) shows all coding and non-coding genes. Diamonds denote probe interaction sites in Micro-c for both the non-TAD probes (red) and the TAD boundary probes (blue).

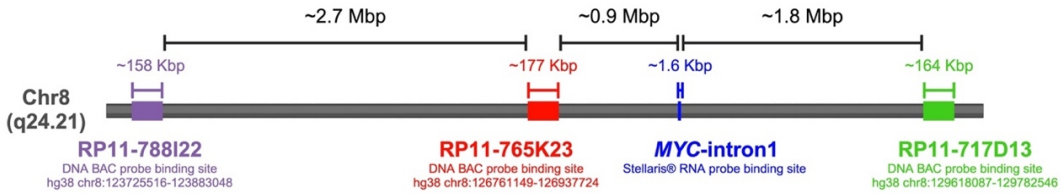

MYC Stellaris® RNA Probes hybridization sites

(Intron1, hg38 chr8:127736231-127737854, strand: +, 5' to 3')

gtaagcaccgaagtccacttgccttttaatttattttttttatcacttt**aatgctgagatgagtcgaat**gcctaaataggggtgtcttttctcccattcctgcctattgacactttt**ctcagagtagttatggtaa**ctggggctggggtgggggggtaatccagaactggatcg**ggggtaaagtgacttgtcaag**atgggagagggagaaggcagagggaaa**acgggaatggtttttaagac**taccctttcgagatttctgccttatgaatatattcacgctgactcccggcc**ggtcggacattcctgctttt**attgtgtt**aattgctctctgggttttgg**gggggctgggggttgctttgcggtgggcagaaagccc**cttgcatcctgagctccttg**gagtagggaccg**catatcgcctgtgtgagcca**gatcgctccgcagccg**ctgacttgtccccgtctccg**ggagggcatttaaatttcggctcaccgcatttctgacagccggagacggacactgcggcgcgtcccgcccgcctgtcccccgcggcgattccaa**cccgccctgatccttttaag**aagttggcattggcttttaaaagcaataatacaatttaaaacctgggtctctagaggtgttaggacgtggtgttggggtaggcgcaggcaggggaaaaggggaggcgaggatgtgtccgattctccttgaatcgttgacttggaaaaaccaggcgaatctccgcacccagccctgactcccctgccgcggccgccct cgggtgtcctcgcgcccgagatgcggaggaactgcgaggagcggggctctgggcggttc**cagaacagctgctaccctt**ggtggggtggctccgggggaggtatcgcagcggggtctctggcgcagtt**gcatctccgtattgagtgc**gaag**gggaggtgcccctattattat**tttgaca**cccccccttgtat ttatgga**aggggtgttaaagcccgcggctgagctcgccactccagccggcgagagaaagaagaaaagctggcaaaaggagtgttggacgggggcggtactgggggtggggacgggggcggtggagagggaaggttgggaggggctgcggtgccggcgggggtaggagagcggctagggcgcga gtgggaacagccgcagcggaggggcccccggcgcggagcgggggttcacgcagccgctagcgcccaggcgcctctcgccttctccttcaggtggc**gcaaaacttttgtgccttggatt**ttt**ggcaaattgttttcctcaccg**c**ccacctcccgcggcttctttaa**gggcgccag**ggccgatttcgattcctctg** ccgctgcggggccgactcccgggctttgcgctccgggctcccgggggagcggggctcggcgggcaccaagccgctggttca**ctaagtgcgtctccgagata**gcaggggactgtccaaaggggtg**aaagggtgctccctttattc**ccccaccaagaccacccagccg**ctttaggggatagctct gca**aggggagaggttcgggactgtggcgcgcactgcgcgctgcgccaggtttccg**caccaagaccccttttaactc**aa**gactgcctcccgctttgtgt**gccccgctccag

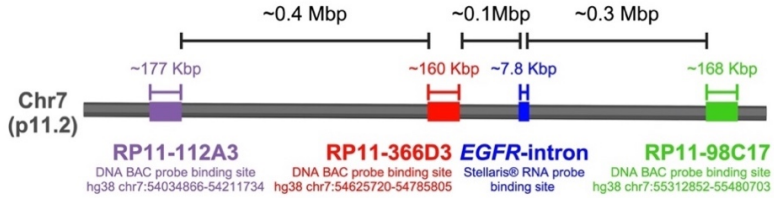

EGFR Stellaris® RNA Probes hybridization sites

(the initial 7,843 nucleotides of Intron1, hg38 chr7:55019366-55027209, strand: +, 5' to 3')

gtaagggcgtgtctcgccggctcccgcgccgccccggatcgcgccccggacccccgcagcccgcccaaccgcgcaccggcgcaccggctcggcgcccgcgccccgcccgtcctttcctgtttccttgagatcagctgcgccgccgaccgggaccgcgggaggaacggg**gacgtttcgttcttcggccg**ggagagtctggggcgggcggagaggaagacgcgtgggacaccgg gctgcaggccaggcggggaacggcgcgcgggaacctccggcgccccgaaccgctcccaacttttcttccctcactttcccccgccagctgcgcaggatcggcgtcagtgggcgaaagccgggtgctggtgggcgcctgggccggggtcccgcacgtgcgcccccgcgctgtcttcccagggcgcgacggggtcctggcgcgcacccgagggcgcggcgtcgcccacccgccgagac tgcactgtttagggaagctgaggaaggaacccaaaaatacagcctcccctcggaccccgcgggacaggcggctttctgagaggacctccccgcctccgccctcccgcgcaggtctcaaactgaagccggcgcccgccagcctggccccggcccctctccaggtcccccgcatcctcgttccccagtgtggagtcgcagcctcgacctgggagctgggagaactcgtctaccaccacctg cggctcccggggagggggtggtgctgg**cggcggttagtttcctcgtt**ggcaaaaggcaggtgggggtccgacccgcccctgggcgcagacccccggccgctcgcctcgcccggtgcgc**ccctcgtcttgcctatccaag**agtgcccccacctcccggggacccccagtccctcctgggcgcccgcgcgaaagccccaggctctcctcgatggccgcctcgcggagacgtccgggt ctgctccacctgcagccctcggtcgcgcctgggcttcgcggtggagcgggacgcggctgtccggccactgcagggggggatcgcgggactcttgagcggaagccccggaagcagagctcatcctggccaacaccatggtgtttcaaaatggggctcacagcaaacttctctcaaaacccggagacttttcttcttggatgtctcttttgctgtttgaagaatttgagccaaccaaaatatta aacctgtcttacacacacacacacacacacacacacacacccggattgctgtccctggttcaagtgtgccaagtgtgcagacagaacatgagcgagtctggcttcgtgactacc**gaccataaacccacttgac**aggggaa**aacatgcctggaaggttta**attgcacaattccaaccttgagctgcgcgggttccaagagccaggcccgtactt**gctgttgatgtcattggctt**gg ggagttgggggtttggtgcccagcgcggtcgttggggaggggcaaggcatagaacagtggttcccagacctgctgcacattggaattacctgggattaaaaaaaaaaaaatcaaaacaaaaaccagtgtctggctcccgcccccagacattctgatttaattggcatgggcaagacctggactggaattttttttaatgctcttcatgtgatctgttgggcagccagatttggggatcactag acggaagaaggattgttaaagtctccggagatgttacttgccaatgctaagagctc**tttgaggacatctggaattgt**tacaatattgccaaaatatggaaagagggaaaaggtagagtgtgattccaataataaaggattccgcttttcattgaaggaac**ggtggaaaggtttcttctc**tgctgagcctgcaggcccgtcctgcctgcctggggtgcccgggagacgcgggcctgctccgg agactgctgactgccggt**cctgttagtcaggtgtcag**ccctgtctctgccgaagagactcttctctttttttaaattaaaccctcagagcaccaccaaagcatcacttttctccctccattggtgttctcattctttgatgttactttgtttgaacaccactattagtagttggagatttgttcctgagaaaaataataaccacttaatttgcctgtttgtcccgcatt**cactcaaaacagaatgctccc**tgaag acaagagagagagtaggagaacagacgctattccattacagtaacataaaagact**ggattttcaggggcaaatta**ttaaaataggagatgagctctttttaacagaaatttgtttaaggcctgtgtctatcaaattcagtggattttattcaagatgcacttttgtttagtgggagttttgttttg**gttctgggacatgctaactt**ctag**actgctgctcttagaggt**aatgactgccagacaccatttca tgagtcctaatccccacattaagcataagaggtgcacactctcctcctatgggggaaactgaggtacgaagaactaaagtgacttttcccacagctggtgggaggcagacgggaaattcacaccaggggcttccaactccagatccctctctcaacttccaaactccactgccttgtccgagttctggtttcaggagatcc**aaatcaggtgtgtgcaaatg**tctaatgtcagagctggcaagggg gaaagggcccagggagccggctcatgacgatgagcctgctgaagcttcaacgcgggctgtccggcagtctgcattcctgcc**gagttcctcagccctctgtt**gggtcaccttccatagaggcagcttagtcctcagttcagtgagcatggagtggagactgcttgaggggtgctgagcaaagccctgcctcttacaggatgaaggtgctctccagaagggacactggaaagtattccaag gc**gagtcgaattcccaactgag**ggagctttgtggaaataagcccgcccagcccccacttct**ggagacgttcccattcagta**ggt**ccgagctgtcttaaagag**aaaccaaagtgggaatattaatggtatccaaagtgagatcacccccacctcccctcctcaaaggaggtcagatcaagaaagcccaagcccggcctggcaattgggacctttctctcacccagcccagggtgaa ggtggacaagtc**actttgacccttcaggcttc**tgagctgttgtttctgaattcagtgaatatttactgagtgcatagaatatgctagatattctgggctaaaggttgaaggggggggtgagttt**aaggtttctgctcttgctt**ccagattgctttcaaatctggaaaggacaccagtggtttgtgttagaccccacactgccgtag**cacagaatacaagaaactgg**ctgagagctccaataggct tttaacagtaatttctggcttcacgtatttagtttcataactcatgattttcaaaaacttctggtttgaagacacc**gattgccgaaagtccatt**gtgctgcataattacacttggtccacgtgacagcactaacatgtttctgaaatgtttttagaagtagtctcagcaaagatgaaggattcctccctgtttgaaaagaaaatattctttgtttttctttgatctaagctctaagactagcagctagcatctgaaa ctttttgac**gagagtgacaaaccaactcta**atattaaag**caattgatgattatgggca**ctgaagggaaggtaaccccaggctggtgcccccggaatagggatgggtcacaat**gttgaggacatttcgcctgtt**gcagaacccacctgcaacacagtgtggccctgccatgtgacttgtgtgtgtgcctgtttttaatttttgactcataagtactctagttatgagctt atttaacattgggttttactaataggggtatgtgttgagaaaatttcaaagttttagaatatg**gttcacccacatgttgcttc**cctgtaaatataattttttaaaaccagatttcgggccgggcatggtggctcacctctataatcccaaaacgttgggaggccgaggcaggcgaatcatgaagccaggagttttgagaccaggctgaccaacacggtgaaacccagtctctactaaaaatacaaaaa aaattagctgggcgtggtggcaggtgcctgtaatcccagctactcaggaggctgaggcaggagaattgcttgaacccaggaggcagaggttgcagtgagccaagatcgcaccattgcactccagcccgcgcgacagtgtgagactccatctcaaaaaaaaaaaaaaaaaaacagattctgttcctcagatccattccatttttgttttccttttatcacttatgggacatttgaaattatggtaataa acattgttagtctcagttaattattactggtttatttcttgaaccactaatccatagagaatagagtgtaaatctt**aacttgttcctgtaggccat**ccccattaaacatcatagtgttttctcattcgttctttttcgtttctcctctacaggaatgaattttctaagaaaattccagcagttggctctt**ggacgacatctctagattg**tcctccattgggcccataggcacaagctggccagtt**tgaatttgggca agaatcc**aggcattggaacttattcaaataactagtttgcctgtaatttttcacttttcagagtcatctgataaagctttcttgctacacatttagatagatacactcaatccagttgtctagaaagttccctgagccagctgggagcaggaggggtagttggggccaggaatattggggg**tgtgtttactgagcccctaga**aagtaagtgctagatttgacatttcaatccctgaaggccctgaagttc agtatcaaatgactggtcctgtggactgagcatctgtgaattgcatatgcttagagtaaatttt**tactcctaccagtttcagcag**cttgcttagcaagcagtatggaaacactaacatgggggagtagaatttctctctctgatccaagtttatctctctctgaatatatctggaacttcctgtgcatccatatgttgagatgtaagaataa gggacaaggcacccaatgagaatgcctgcaggcagccctaagtacacctgcaattacaccattactagcgcggcagcac**acatggccctgacttagttt**aaataattacgtaagtcaaccatgattgtttgcccttgcatagaagggcaagtattggtacctgttacaactaggctttttttctttatgtttgagccatgatgagtgatttacactgttgcatccatatgttgagatgtaagaataa attagacttggta**attgcccttaagtgtctgga**agtcaactggggaaagagagctagagataataagtgtgaaacaatgtcacagaatcaatgacggaactcttccc**aggacaaaggatgacttttg**agttcagtctttt**gccttttaattctacatggggg**aggagagc**cagtttagccacaaatggaa**gggattactcatttgagctatttggttatatgattatttccccagagaataggatg tgcagggcattacacaagcagtgccaatagcagcaaagttcttgagagtgctagtaattcaaatggcaggaagaagaaggataaatggtaaggctacctacagttcacagagagctcatcctcactgtggctttggattttgtcctgtgtgaaagagaagtgactgtgaacatgctgtgtttggtgtttttagaaagatggctgcagcagcggttttgggaatggactgcaggagtggcat tggaaacaggaaggttcatgactattgccagagacagaggatgaagcaggagcaaggaagattcaggacaggggactccggggctgatcaggaggcagaactggttgataagatatatgtagcagcataagaaagaaagaatcccagattgacacccaggcttctcacttggaagcctggatagatactgaatgcaatcacaaaggctgggaagtcaatgggactgcagggaagg gaagggaagggaggagaagaggaagggcaggagggtccaatatcaatattcagctttagatgtgttgacttgaagtgctcagatggagaagtccaggaggcagtagaatacggtggtccagagcacaggagacgaatgtggcttgagttgtcatttgctcacatatttccgtgtcagttacttgtcttagatcacagaacaagttctc**ctctcacagtttcctggctc**cacctgtctcatgct **cccgtcagcatcgaaattgag**ccacaccaggggtt**ctggataccagcttctctct**aggtgaggctgctatagt**cagcagctgattagttgcag**ttatcagcaactggtaaatataatatattgtgcatataagtgtaccagaagtcatgtttatatattgctgcaaatactcggaatggggatctctt**gttccctgcttaagaccacat**cacattacttggttttgtacgctagtggctgaacca aaaaaagtaggagatgatttttttctttttctttaaagcagtagcttttgaacctgaccatgctttctaaccagctgaggggcttttgaaaaagagggtgccttactgtgccccagaccaggacaatcagtatttctggggaatggagcctggcacacacacatttcttaaagctcccttggcaattct**gaggagtggattacatgtt**gtatgt**agctcgtaacgaaagaaatc**ttgtctttgctctca **gacccccattt**tcttactcatctcatgagct**ccttcgagatccagaaacag**ttgcatatttcattagtaaatcagttccagagtcacattttaatttcacaagttagtccattaaaagtttcctgcagtgaggaaatagccagaaagaacactccaccccctcctccttttataactataggggtctggctcgacagagcaggagcatcgccatcttggacaagccctcaattctaaagttcacctttaataaa aaactgcctaaattcaaactgcatcagcctaatggctaaggtcagcatgaccataaaccacaaataacatctccaaccggaaacattcgaaactcctcctcgaccagagacatgctagtcccgagataacccccctccagcagggaagatgccagtctcgggataacctctctctggccggaaagatgcctgcccaagataaacttgcctcctcccagagatattccaaccctgccata aaacttctccctcaaacaggaacattccaaaattctgataatctccctcacccttaaaaccaatatatactcctagtctgtaagagaaagcgctcttgaccaaaattcaccaggagtgcctcccaggttttaactaaagaaaacctctctttaactgccaaaaaaaaaaaaggggaaaaaaaaaagctttctgcagtggctttcagcgggcccagcatggcagcagcacctgagaacctgttggag atgcacactcttggaccccacccctggcctctgagtaagacactggaagggcaggccccggtctgtgcacacaagtcctcagggagattctgactgatgcatgccagtttgagaactgctgatatactccaggcacatcgcatgctgggatctagatacaccaagggacaaaataactgcacttgtcctctgaggaccgacttacctttggaagggctgagaaagagagacacataca agatcactccctgt

Supplementary Figure 2. Sequence and location of DNA and RNA probes binding sites for DNA/RNA HiFISH

Top: schematic representation of target regions. Oligonucleotide targeting sequences are indicated in blue. Bottom: target sequence regions.

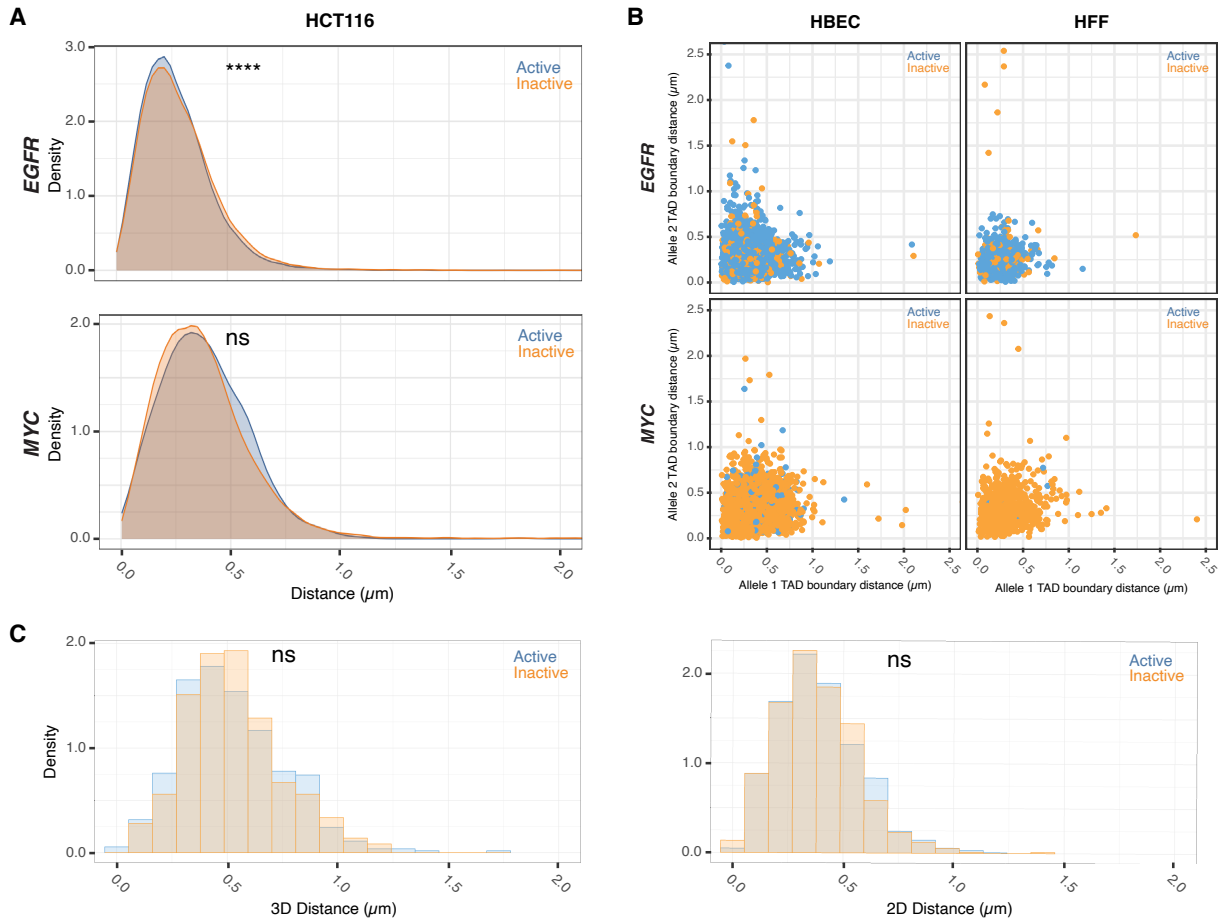

Supplementary Figure 3. TAD boundary proximity is uncoupled from allelic gene activity in single nuclei in both 2D and 3D imaging

(A) *Comparison of TAD boundary distances for EGFR and MYC alleles in HCT116 based on transcriptional activity status. Histograms of allele-specific distance distributions from a representative dataset from a single experiment. Mann–Whitney U test p-values are indicated as follows: ****p < 0.0001; ns, not significant (p ≥ 0.05).*

(B) *Comparative analysis of TAD boundary distances between active and inactive alleles within the same nucleus for EGFR and MYC loci in HBEC and HFF cells.*

(C) *Comparison of TAD boundary distances for MYC alleles in HBEC based on transcriptional activity status, measured using both 2D and 3D imaging. Histograms show allele-specific distance distributions from a representative dataset of a single experiment. Mann–Whitney U test p-values are indicated as follows: ns, not significant (p ≥ 0.05).*

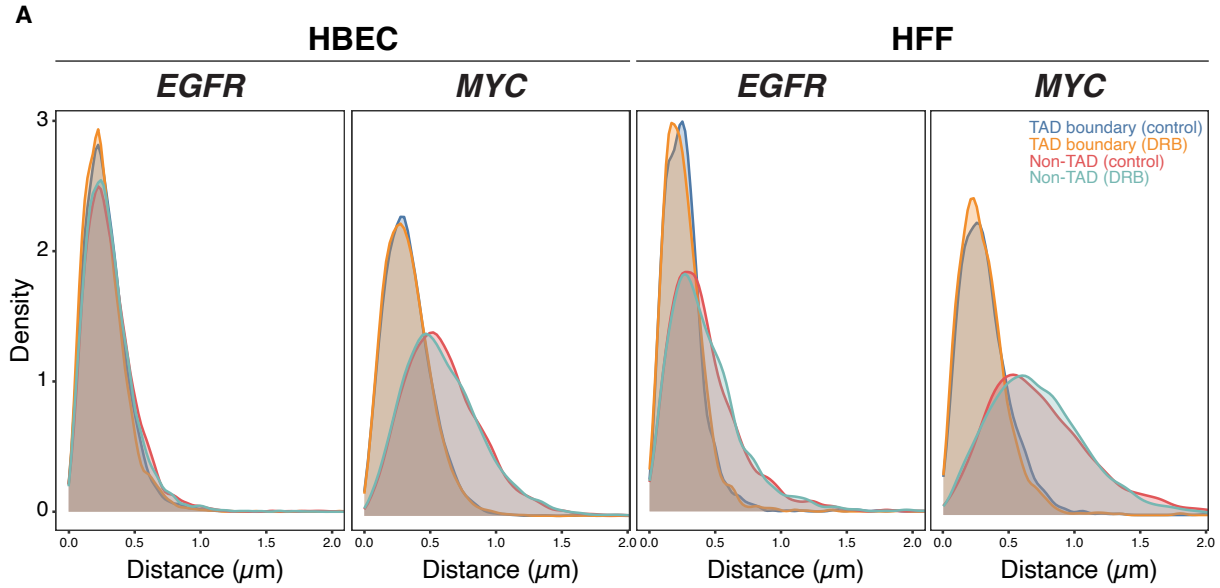

Supplementary Figure 4. Transcriptional inhibition does not affect the spatial organization of non-TAD control regions

(A) *Comparison of TAD boundary and non-TAD distances for EGFR and MYC alleles in HBEC and HFF based on transcriptional inhibition status. Histograms show allele-specific distance distributions from a representative dataset of a single experiment.*

A

Gene	2h Dex fold_change	4h Dex fold_change
EGFR	1.023666933	1.03900346
MYC	0.94073356	0.942055814
ERRFI1	4.21958045	3.046223714
FKBP5	3.601279644	8.110225204
VARS2	5.465222715	6.468733565

B

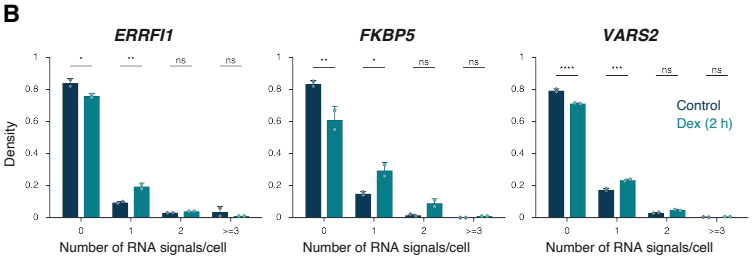

Supplementary Figure 5. RNA levels following DEX treatment

(A) *RNAseq analysis of ERRFI1, VARS2, and FKBP5 RNA levels following Dex treatment for the indicated durations in HBEC cells. Values were calculated RPKM fold-change (Dex/No_Dex) ratio. Data represent the mean of three independent experiments.*

(B) *Histograms of the distribution of nascent RNA transcription sites per nucleus in HBECs upon Dex treatment. Data represent values from at least two independent experiments (diamonds and circles); diamonds (EtOH control) and circles (Dex 2 h) represent the mean of means, and error bars indicate SD. P-values from two-way ANOVA with Bonferroni correction are shown as: ****p < 0.0001; ***p < 0.001; **p < 0.01; *p < 0.05; ns, not significant (p ≥ 0.05).*

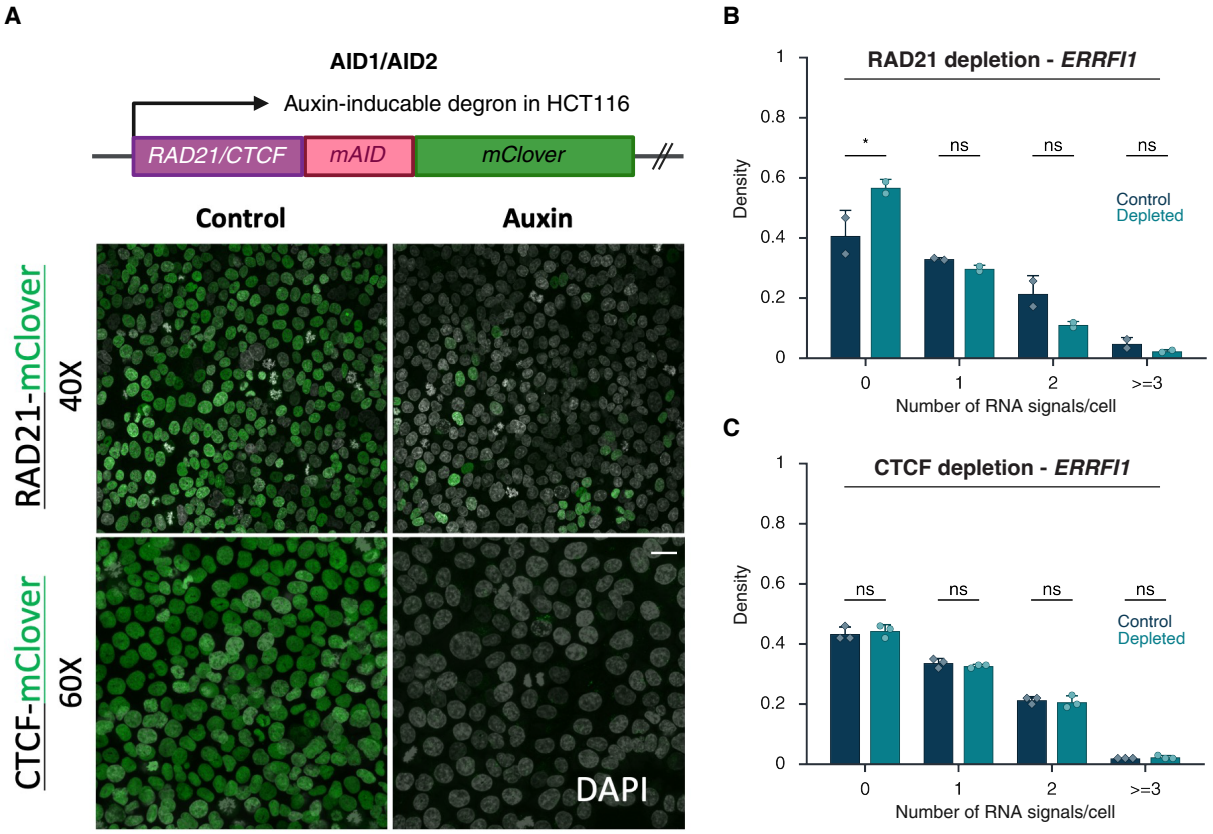

Supplementary Figure 6. Depletion of RAD21 and CTCF

(A) *Loss of RAD21 or CTCF in HCT116-RAD21-AID1 or HCT116-CTCF-AID2 cells, respectively, following DMSO (control) or auxin treatment. RAD21 and CTCF degradation were assessed using mClover- fluorescence (green). Scale bar: 20 µm*

(B-C) *Fraction of silent (0), monoallelic (1), biallelic (2), and triallelic or more (≥3) expression of the indicated genes in individual cells after 3 hours or no auxin treatment in HCT116-RAD21-AID1 (B) or HCT116-CTCF-AID2 (C) cells. Data represent values from at least two independent experiments (diamonds and circles); diamonds (DMSO control) and circles (RAD21 or CTCF-depleted) represent the mean of means, and error bars indicate SD. P-values from two-way ANOVA with Bonferroni correction are shown as: *p < 0.05; ns, not significant (p ≥ 0.05).*